CHALMERS

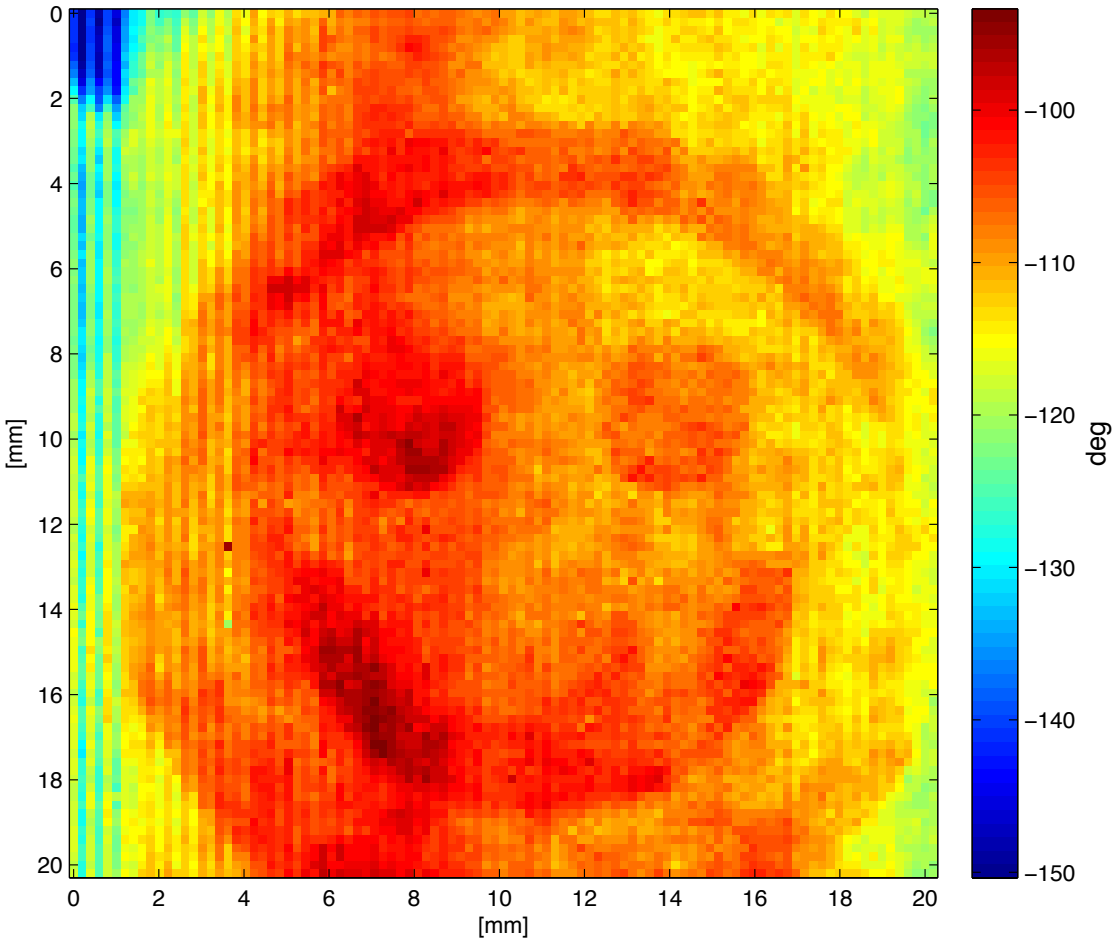

Sub-millimetre wave imaging

Thesis for the degree of Master of Science in Wireless and Photonics Engineering

ROBIN DAHLBÄCK

Terahertz and Millimetre Wave Laboratory
Department of Microtechnology and Nanoscience
CHALMERS UNIVERSITY OF TECHNOLOGY
Göteborg, Sweden, 2011

Thesis for the degree of Master of Science in
Wireless and Photonics Engineering

Sub-millimetre wave imaging

ROBIN DAHLBÄCK

Terahertz and Millimetre Wave Laboratory
Department of Microtechnology and Nanoscience
Chalmers University of Technology
Göteborg, Sweden, 2011

Sub-millimetre wave imaging

©ROBIN DAHLBÄCK

Terahertz and Millimetre Wave Laboratory
Department of Microtechnology and Nanoscience
Chalmers University of Technology
SE–412 96 Göteborg, Sweden
Phone: +46 (0)31–772 1000

Cover: Phase contrast of a laser printed paper imaged at 340 GHz, see section 6.3.3

Printed in Sweden
TeknologTryck
Göteborg, Sweden 2011

Abstract

The sub-millimetre wave region withholds many interesting properties that can be used for imaging. Common packaging materials are transparent making package inspection possible without the use of ionising radiation. Contrast can also be seen between healthy and diseased tissue for some common forms of cancer. Many other biomedical applications are still unexplored making it an interesting research topic. A study of common system topologies are presented together with an imaging system built with in-house components. The imaging system is adopted for the use of a microwave tomography image reconstruction algorithm. System characterisation data are presented, the usable bandwidth is 6.5 % centred around 337 GHz. Measurement repeatability and long therm stability is also evaluated, concluding that the system most likely is good enough for use with the image reconstruction algorithm. Furthermore test images are presented.

Preface

This report is the result of a 60 *hec*, higher education credits, master thesis carried out at Chalmers University of Technology, Department of Microtechnology and Nanoscience, Terahertz and Millimetre Wave Laboratory. Jan Stake is the main supervisor and examiner and Tomas Bryllert is co-supervisor. The project is part of the SFF sponsored project Charmant Medical THz which also involves Tonny Rubaek, Mikael Persson and Andreas Fhager from the Biomedical Engineering Division, Department of Signals and Systems.

Acknowledgements

This work would not have been possible without the preceding efforts and guidance of Dr. Biddut Banik. I would like to thank my supervisors professor Jan Stake and Dr. Tomas Bryllert for their help and guidance. Dr. Peter Sobis has been my mentor in the practical work and also a great source of both ideas and components. The entire staff of the Terahertz and Millimetre Wave Laboratory deserves recognition for providing such an inspiring and pleasant working environment. Finally, I would like to thank The Swedish Foundation for Strategic Research, SSF, for funding this research.

Contents

1 Introduction

Terahertz frequency radiation is typically defined to be in the region $0.1 - 10\,THz$. Since it lies between the infrared and microwave regions in the electromagnetic spectrum it has many interesting properties that can be useful for imaging purposes. Common packaging materials are transparent making non invasive package inspection possible without the use of X-rays. Cancerous tissue show a contrast in permittivity compared to healthy tissue making the wavelength range an interesting candidate for future medical equipment.

THz imaging has the potential to have a wide range of medical applications where it can improve and aid the detection and diagnosis of disease. One example is a non-invasive method for detection of skin cancer. Time domain systems have been tested to examine different skin properties, [1], however some of the areas that can be improved are SNR and spectral resolution. Areas where frequency domain methods have an advantage. The system being built operates as a CW heterodyne system thus providing good SNR and spectral resolution. The image reconstruction will be done using a microwave tomography algorithm adopted for use with the sub-millimetre wave hardware. The image reconstruction algorithm provides the possibility to have sub wavelength focusing with a large focal depth, thus eliminating common problems with short focal depth and specular reflections.

Other examples of possible areas of implementation is non invasive sensing and inspection in industrial processes or product verification. More general information regarding the wavelength region 100 GHz to 1 THz as well as more specific properties that are interesting for imaging can be found in [2].

The thesis is a part of a collaboration between MC2, S2 and Sahlgrenska in the research centre SSF Charmant.

The purpose of the thesis can be split into two tasks. To investigate previous work and technology within the field of THz imaging and to create an imaging system using in-house available components.

Cell slides containing cancer samples will be available through the collaboration with Sahlgrenska, making a sub-millimetre wave image of the available samples is one of the goals of the work.

1.1 Thesis layout

The following short summary of the different sections is intended to serve as a guide to the reader:

- Section 1 gives an introduction to the work and presents the goal.
- Section 2 gives a background and lists several imaging systems constructed by other groups. System topologies are summarised together

with some common techniques for image formation.

- Section 3 lists some of the properties making the sub-millimetre wave region unique. Finally some theory concerning the constructed system is presented.
- Section 4 describes the evolution of the imaging system being built. Various components included in the system are also described.
- Section 5 presents measurements done in order to evaluate the constructed system.
- Section 6 presents the results together with some images created during the work.
- Section 7 summarises the work and the conclusions.
- Section 8 presents thoughts about possible future continuation of the work.

1.2 Goals and requirements

The goals of the work are listed below:

- Investigate what can be done with in house available equipment.
- Test sub millimetre wave imaging using available equipment.
- Publish a scientific article within the topic.
- Characterise previously manufactured catadioptric lens at $340\,GHz$.
- Image the cancer samples available through the collaboration SSF Charmant.
- Summarise previous work within the field.
- Summarise different common technologies.

The requirements that needs to be completed are:

- Test sub-millimetre wave imaging using available equipment.
- Characterise previously manufactured catadioptric lens at $340\,GHz$.
- Image the cancer samples available through the collaboration SSF Charmant.
- Summarise previous work within the field.
- Summarise different common technologies.

1.3 Delimitations

The work should be finished within one academic year corresponding to 60 *hec*. Available equipment should be used to as large extent possible, new equipment can be bought if the cost is low or if it can be reused in other projects.

Concerning the summation of previous work within the field the study will be limited to systems and applications that share some similarities with the constructed system, either in construction or in the field of application. There ere already several excellent articles aiming at summarising the whole field of THz imaging, see for example [3], [4], [5].

2 Background

This section will give a brief background to the concept of THz imaging and present a number of different THz imaging systems. A more detailed description of the operation of the different systems are given in section 2.1 and 2.2.

Imaging can generally be done in passive or active mode where the first relies on detection of an existing signal while the second illuminates the imaged object and records the reflection or transmission. As indicated two common forms of imaging are reflection and transmission imaging. In transmission imaging the signal transmitted through the imaged object is detected while reflection imaging detects the signal that the object reflects.

There are a huge number of imaging modalities, in this thesis emphasise will mainly be placed on system used for biomedical examination and hidden objects detection.

2.1 Passive imaging systems

This section will give an introduction to passive sub-millimetre wave imaging. Requirements on radiometer systems operating with a high background temperature will also be briefly discussed.

When doing passive imaging the contrast in the scene will arise from the different radiometric temperatures in the scene. In a simple view of it the parameters affecting the effective radiometric temperature, T_E, are the physical temperature of the object, T_O, the emissivity, ϵ, the reflectivity, ρ, and the radiometric temperature of the surrounding illumination, $T_{ILLUMINATOR}$ [6]. The equation for the effective radiometric temperature can be written as:

$$T_E = T_S + T_{SC} = \epsilon T_O + \rho T_{ILLUMINATOR} \tag{1}$$

Where T_S is the radiometric temperature and T_{SC} the scattered radiometric temperature. The radiometric temperature is simply the product of the emissivity and the objects physical temperature. The emissivity is a function of the dielectric properties of the material, the angle of observation, the surface properties and is also polarisation dependent.

$$T_S = \epsilon T_O \tag{2}$$

The scattered radiometric temperature is the product of the reflectivity and the radiometric temperature of the background illumination. Outdoors the sky is usually the main source of background illumination and the sky radiometric temperature is discussed in section 3.1 but is in general much colder then surrounding objects at sea level.

$$T_{SC} = \rho T_{ILLUMINATOR} \tag{3}$$

One common situation in passive sub-millimetre wave imaging is when a smooth metallic object, $\epsilon \approx 0$, is placed in front of something with much higher emissivity i.e a knife hidden under clothes or a vehicle in front of vegetation. For an indoor scene the metallic object will be seen as a shadow on a background with higher radiometric temperature if the object is held close to the skin and specular reflections from objects with higher radiometric temperature is avoided. Outdoors the metallic object is likely to reflect the cold sky thus appearing to be colder in both scenes.

2.1.1 Radiometers

Cryogenic state of the art radiometers operate with equivalent noise temperatures much lower than the warm background seen in ground based imaging situations. Room temperature receivers can therefore be employed in many passive imaging scenarios by allowing a longer signal integration time. An example of a passive image of a human holding a wrench can be seen in Figure 1. The image thermal resolution is $0.25\,^{\circ}C$ and it is acquired using a room temperature Schottky mixer operating at $640\,GHz$ with a $10\,ms$ integration time for each pixel [7].

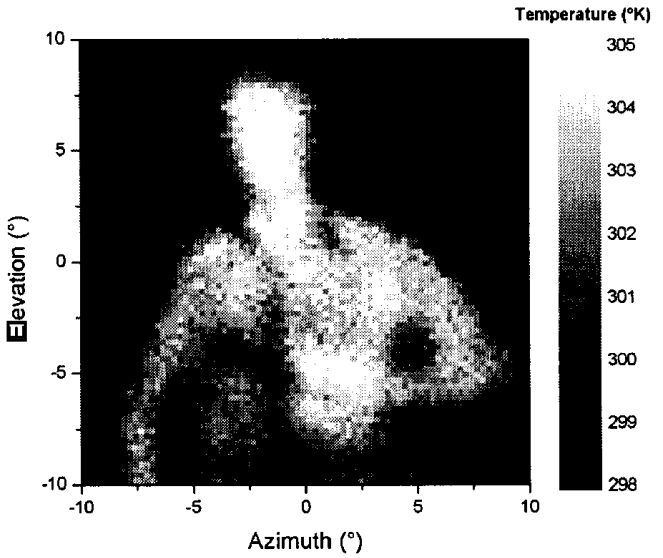

Figure 1: Passive thermal image of a human holding a wrench, acquired with a $640\,GHz$ Schottky mixer[7].

A sensitive passive system built around a hot electron bolometer is presented in [8]. The setup operates by heterodyne detection at $850\,GHz$ and

can clearly resolve a 1 K temperature difference between two pieces of absorber.

2.2 Active imaging systems

In active reflection imaging the picture is largely dependent on specular reflection, especially when it comes to metal objects with a surface roughness that is small compared to the wavelength. In such cases the the angle of incidence of both the transmitter and receiver is critical and the reflection is only seen in a narrow viewing angle.

Transmission imaging on the other hand is mostly limited by attenuation through the sample. Samples containing water or other polar liquids tend to be very lossy while many dielectric materials that are opaque in the optical region show relatively small loss in the THz region, a more detailed discussion of sample properties can be found in section 3.1.1.

By employing modulation techniques that enables range finding, i.e. the FMCW technique described in section 2.2.2, the dependance of the surface reflectivity can be greatly reduced since the returned signal only needs to be detectable within the instruments dynamic range in order to find the distance to the target.

2.2.1 Multiplier based systems

There are more or less two approaches to sub-millimetre wave imaging. When using microwave techniques the challenge is to increase the frequency. When an optical approach is used the problem is the opposite.

Due to the lack of good fundamental electronic oscillators in the region above some GHz a lower frequency signal is typically multiplied in a non-linear device called a multiplier. The fundamental principle of the multiplier is that if signal is feed to a non linear device the output will contain harmonics of the input signal. By proper filtering the desired harmonic can be extracted an used. Common non-linear devices used in the THz region are Schottky and HBV diodes.

As receivers both bolometers and Schottky mixers are common. Depending on the system properties required the receiver topology may vary from direct detection to heterodyning. The receivers are usually configured in single pixel setups due to the difficulty and high cost of multi-pixel arrays. However one emerging technology that might enable cheep focal plane arrays is described in [9].

The simplest form of active imaging is when a CW transmitter is used to illuminate the target and the reflected power level is recorded. An example of such an image is shown in Figure 2 where a person hiding a handgun under a shirt is imaged at 640 GHz. The specular reflection seen from the handgun in the picture is relying on the fact that the image is recorded at

close to normal incidence. A slight shift in viewing angle quickly makes the gun unresolvable.

Figure 2: Active image showing reflected power from a person with a handgun hidden under a shirt, taken at 640 GHz[2].

2.2.2 FMCW range-finding

By modulating the output from the measurement equipment as a linear frequency sweep the distance to the target can be found by the frequency offset created by the signals flight path. This technique is commonly known as Frequency Modulated Continuous Wave radar or simply FMCW radar. The FMCW radars range resolution is inversely proportional to its bandwidth according to [10]:

$$\Delta r = \frac{c}{2\Delta F} \tag{4}$$

Where c is the speed of light, Δr the range resolution and ΔF the chirp radar bandwidth. A radar bandwidth of 100 GHz gives a theoretical range resolution of 1.5 mm.

The range to the target is found by examination of the IF frequency:

$$f_{IF} = \frac{2KR}{c} \tag{5}$$

Where $K\,(Hz/s)$ is the chirp rate and $R\,(m)$ the range to the target. As an example a chirp rate of $250\,MHz/ms$ gives $f_{IF} = 7\,kHz$ at a target range of $4\,m$. With the same chirp rate the difference frequency between two objects separated by 1 cm would be 17 Hz.

One of the commercial vendors of THz imaging systems is SynView GmbH who produces imaging units operating in coherent FMCW mode. The high frequency head operates between $230-320GHz$ giving a theoretical

range resolution of $< 2\,mm$, see section 2.2.2. An example of a suitcase scan is shown in Figure 3 [11]

Figure 3: A package inspection example created using SynViews imaging system [11].

Another FMCW imaging system that uses the range information to improve the image reconstruction is described in [12]. The system used is based on multipliers and operate as a superheterodyne FMCW radar at around $600\,GHz$. For focusing at standoff distances of $4\,m$ and $25\,m$ large off-axis ellipsoidal reflectors are used, the main reflector is moved by a two axis rotational stage in order to raster scan the scene. The system block diagram is reproduced in Figure 4. The measured spot size and range resolution at $4\,m$ is approximately $1\,cm$. Since it is possible to distinguish the distance between multiple reflections a multilayered 3D image can be constructed. Figure 5 shows how signal processing has been used to extract the first interface, shirt, and the second reflection, gun and skin. The image is taken at $4\,m$ standoff.

Another system that uses the FMCW technique for standoff imaging is found in [13]. Besides using the FMCW approach the quasi-optical configuration is quite interesting since it uses a two axis rotating mirror to direct the beam. This allows a scan speed of 9 seconds per image, the optics are reproduced in Figure 6. Here a frequency divider is used used to create the IF reference instead of a multiplier as in the previous system. A discussion about different IF topologies enabling phase measurements is given in section 3.2.3.

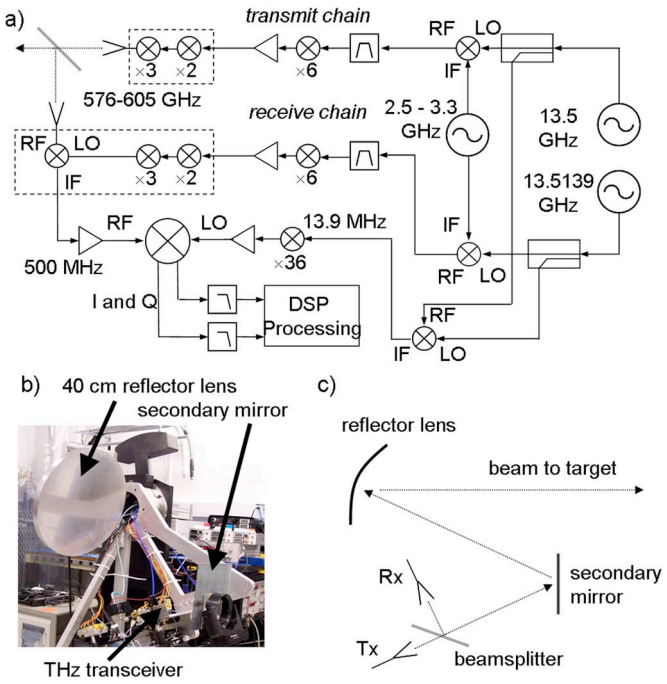

Figure 4: a) System block diagram showing the multiplier based superheterodyne FMCW radar. b) Image showing the setup with the off-axis ellipsoidal main reflector. c) Optics block diagram [12].

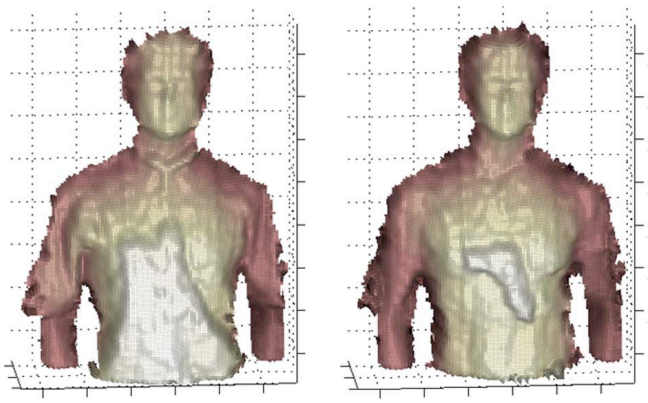

Figure 5: Left: first reflection encountered by the THz beam. Right: First reflection from shirt removed to reveal the reflection from the skin and handgun [12].

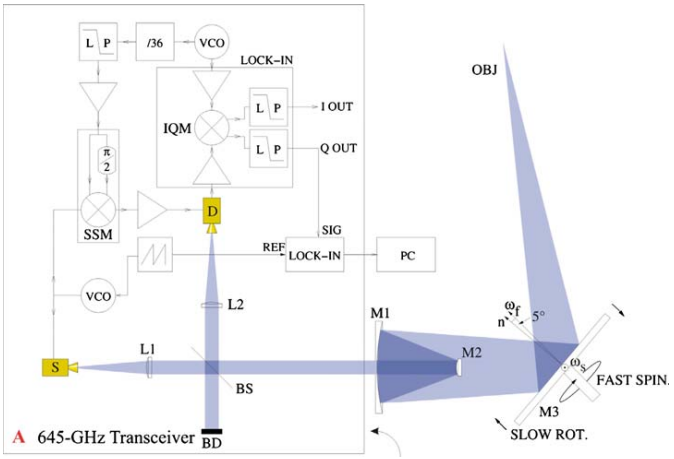

Figure 6: System block diagram together with quasi-optical setup[13].

2.2.3 TPI, terahertz pulsed imaging

Terahertz pulsed imaging, TPI, is probably the most common form of THz imaging. A general THz pulsed time domain transmission measurement system is shown in figure 7. The system works by the principle that short optical pulses excite currents in the semiconductor crystal whereby an electric impulse is radiated with a frequency content in the terahertz region.

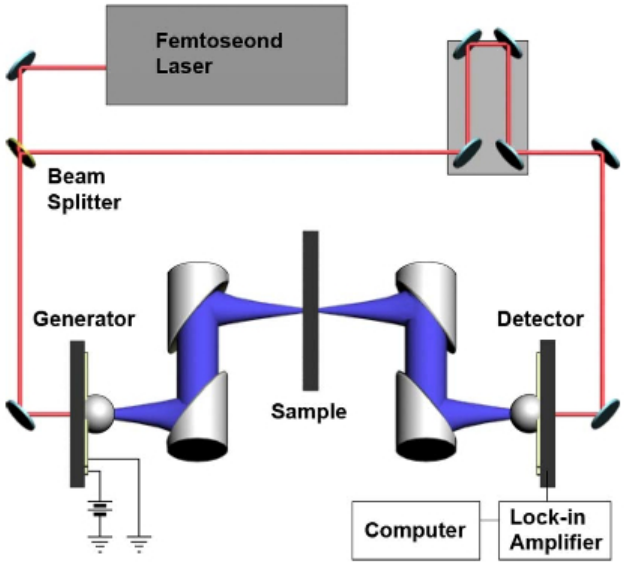

Figure 7: A typical femtosecond pulsed THz measurement system [14].

One of the first reported THz imaging systems are [15]. A pulsed time domain system was used to image an integrated circuit and map the water

content of a leaf. Both images are reproduced in Figure 8 and figure 9.

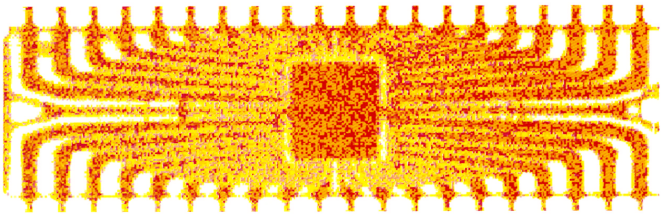

Figure 8: An epoxy packaged IC circuit imaged using a time domain THz imaging system in transmission mode [15].

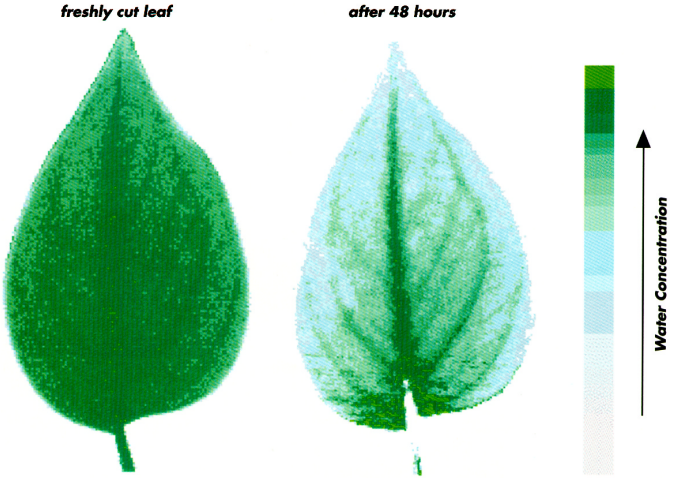

Figure 9: A leaf imaged with a 48h interval showing the difference in water concentration [15].

One vendor of a commercial systems is TeraView who supply systems for both spectroscopy and imaging. Figure 10 shows the system that probably later evolved to one of TeraView's products. It was used in a study where the skin properties of 20 persons where examined by time domain pulse imaging. Three different areas on each person were measured repeatedly during four weeks, one of the results was that the thickness of the stratum corneum of the palm could be measured [1].

One of TeraViews areas of application is inspection of the coating of medical tablets. A system specialised for that task is shown in Figure 11.

A THz imaging study of porcine skin burns is presented in [17]. The contrast in the picture came from a difference in reflectivity between burnt and unburned skin and was detected by a direct detection system operating at centre frequency of $500GHz$ with a $125GHz$, $3dB$ bandwidth. The author also showed that it was possible to image through ten layers of dry medical (cotton) gauze. The system used for the measurements is reproduced in

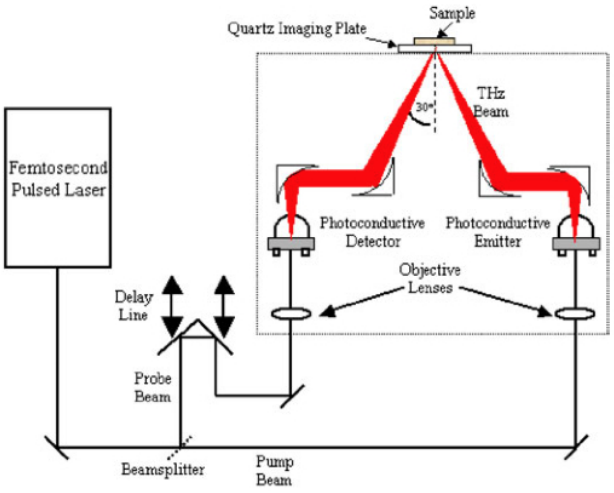

Figure 10: Pulsed time domain THz measurement system used for in vivo studies of human skin [1].

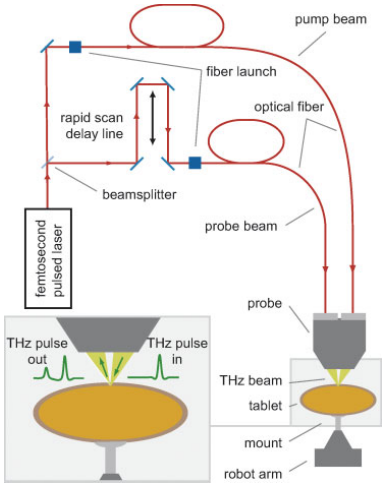

Figure 11: TeraViews TPI system for tablet inspection, note that the THz generation and detection is done inside the probe head [16].

figure 12. The terahertz image of the second-degree burnt skin, imaged in reflection mode can be seen in Figure 13.

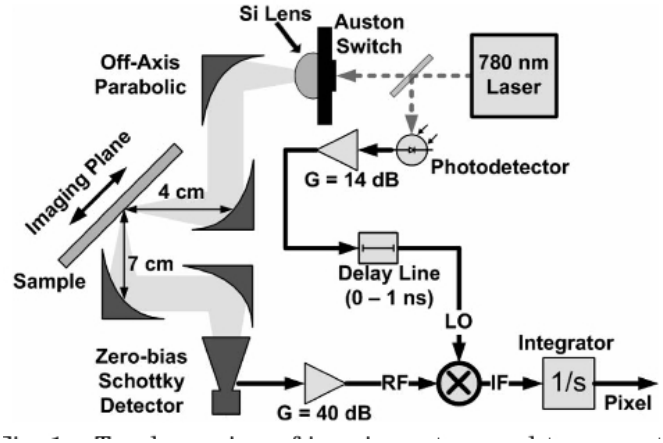

Figure 12: System used to image second-degree skin burns [17].

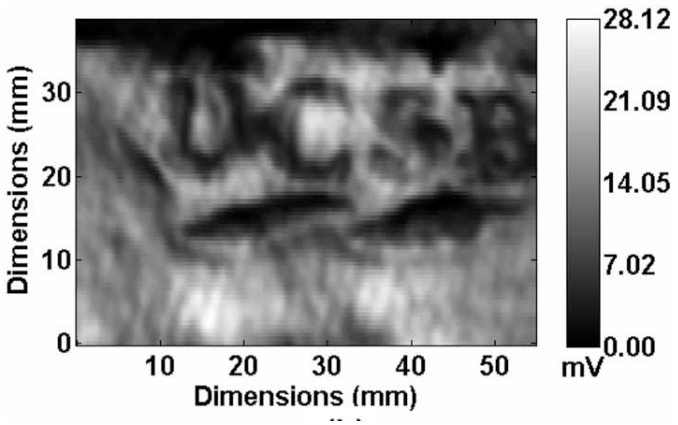

Figure 13: THz reflection image showing a second-degree burn wound [17].

2.2.4 THz imaging by optical beating

An all-optical continuous wave system is described in [18]. The THz radiation is generated by photo-mixing two continuous-wave lasers which then hits the semiconductor that works as THz source. CW transmission measurements of archived cancer samples was performed to demonstrate that the system could compete with state of the art pulsed systems. Since the study was done 2002 it is uncertain if the comparison is still valid. The system is shown in figure 14.

The imaged cancer sample is shown in Figure 15.

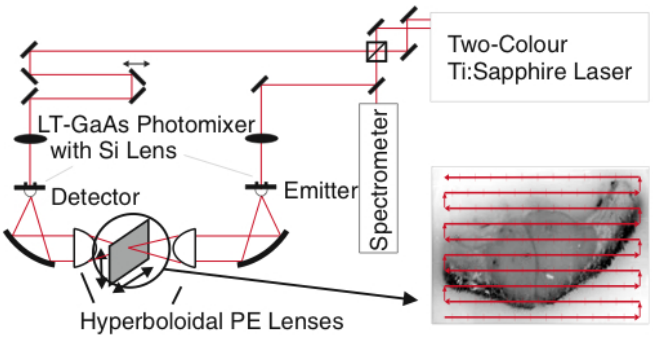

Figure 14: A THz imaging system using the beating frequency of two lasers for THz generation [18].

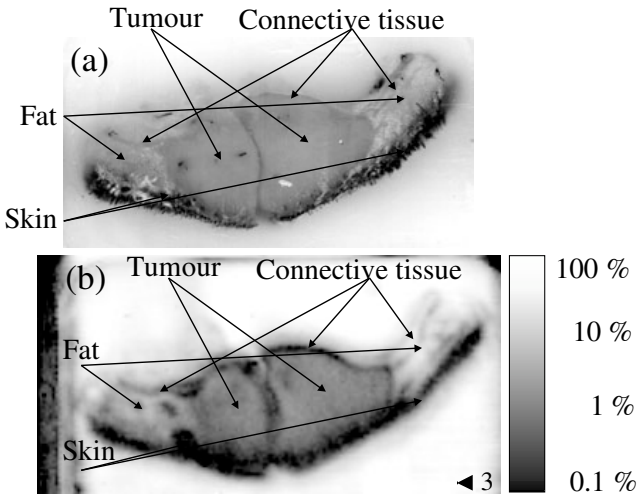

Figure 15: a) A wax-mounted thin-cut canines basal cell tumour, object seise $32x24x3\,mm$. (b) $CW\ THz$ power transmission image at $1\,THz$ [18].

3 Imaging in the sub-millimetre wave region

This section will describe some general properties concerning imaging in the sub-millimetre wave region and give a short description to some of the theoretical background on which the system construction is relying. The imaging properties of water, different types of samples and propagation through the atmosphere will also be discussed.

3.1 Imaging properties in the sub-millimetre wave region

Propagation attenuation through the atmosphere are at many frequencies high in the terahertz region, however some windows exist. Figure 16 shows the propagation attenuation for different weather conditions between $0.1 - 1\,THz$. Fog is a condition in which millimetre wave imaging can have an advantage compared to imaging in the optical region in terms of loss. This is however only valid in the lower THz range since the attenuation above $406\,GHz$ in clear conditions exceeds that of fog in the visible region [2].

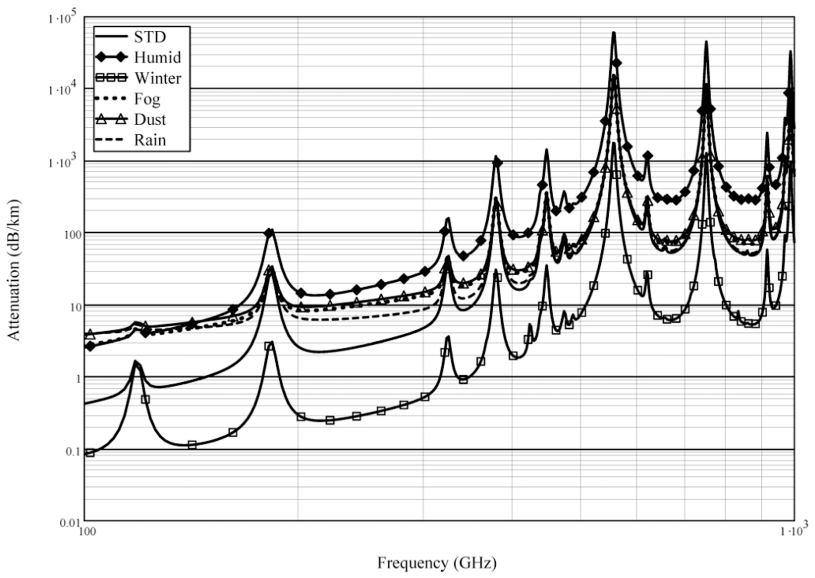

Figure 16: Atmospheric attenuation in the frequency range $100\,MHz - 1\,THZ$[2].

The radiometric background temperature of the sky is associated with loss and is plotted in Figure 17.

Water and polar liquids are highly absorptive in the THz range mainly because of molecular vibration modes. As an example se Figure 18 where it can be seen that the propagation loss through $30\,\mu m$ of de-ionised water already exceeds $40\,dB$.

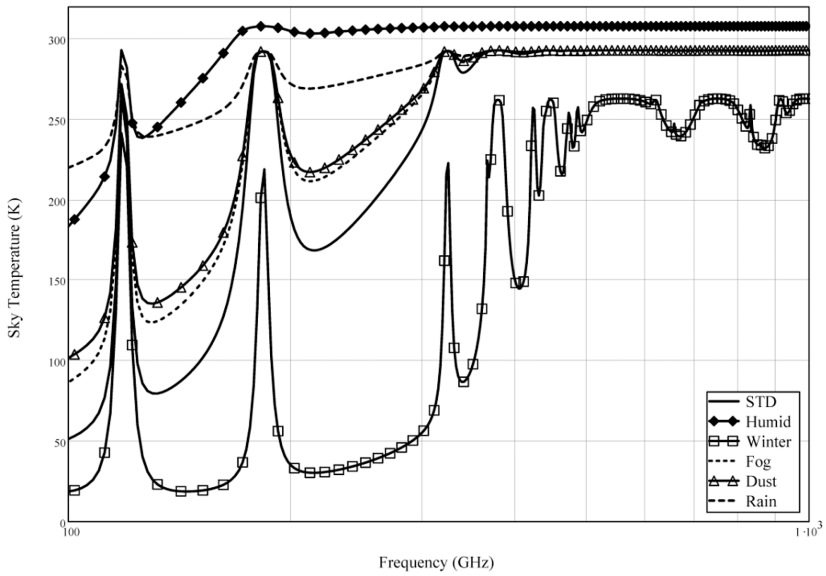

Figure 17: Apparent sky temperature in the $100\,MHz - 1\,THZ$ region [2].

In contrast, dielectrics tend to be transparent in the frequency range making many common packaging materials transparent. This gives an opportunity to perform i.e. non invasive package or bag scans without the use of ionising radiation. Many more examples of non destructive testing and evaluation using sub-millimetre wave radiation can be found.

3.1.1 Electromagnetic properties of samples

Given that water is so absorptive in the THz range medical examination will only be possible at the surface of a biological sample. This means that in vivo measurement are more or less restricted to examining the skin. For ex vivo studies cell slices off different tissues can be examined in both reflection and transmission mode depending on how the sample is prepared.

In [19] cell slides of human breast tumours were examined using pulsed terahertz imaging. It was concluded that healthy tissue could be distinguished from cancer tissue with a correlation to optical examination of $82\,\%$. Cancer samples do in general show a dielectric contrast of approximately $15\,\%$ compared to healthy tissue in the wavelength range.

3.1.2 Sample requirements

In [20] some information about the optical properties of human tissues in the frequency range $0.5 - 2.5\,THz$ can be found. To detect different regions of a sample under investigation contrast in either or both refractive index and attenuation needs to be found.

In order to be able to conduct the measurement the sample need to be thick enough to provide a measurable phase change and still so thin so the attenuation is acceptable. The phase change coming from variations in relative permittivity is further discussed in section 3.2.5.

As seen in [20] the linear attenuation coefficient, $\mu(\omega)$, varies with frequency and type of tissue. The attenuation in de-ionised water is the highest and will therefore be used as reference. At the lowest frequency specified, $500\,GHz$, $\mu(\omega)$ is approximately $150\,cm^{-1}$. Using equation 6 the propagation attenuation of the sample can be calculated. The results can be seen in figure 18. The dynamic range of the measurement system and the measurement mode, reflection or transmission, will determine the required sample thickness. If a transmission measurement is performed through muscle tissue and a $60\,dB$ dynamic range is available the attenuation will most likely need to be less than $50\,dB$ corresponding to approximately $500\,\mu m$.

$$\frac{I(\omega)}{I_0(\omega)} = e^{-\mu(\omega)\cdot d} \tag{6}$$

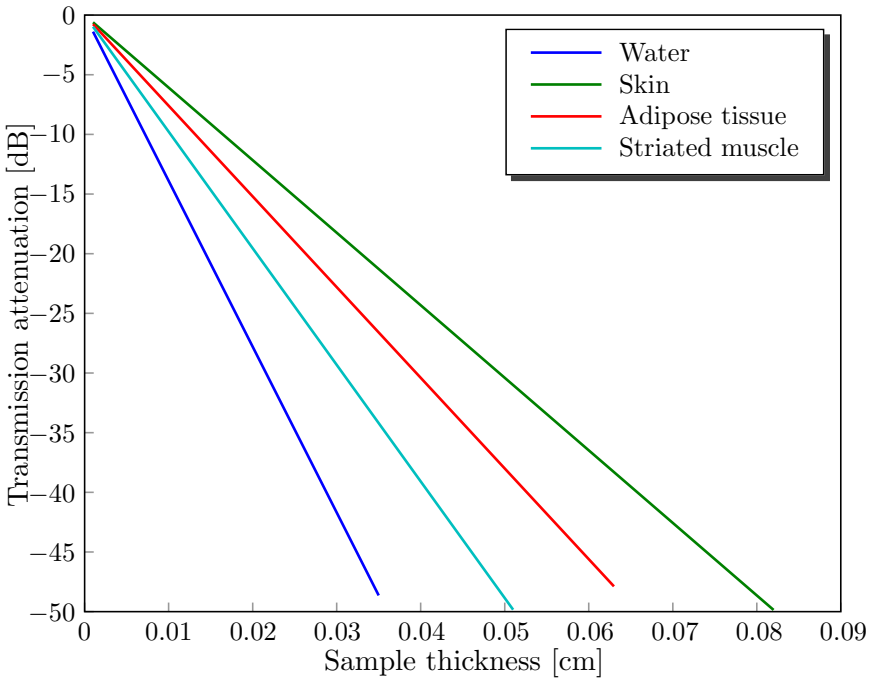

Figure 18: Transmission attenuation through different tissues.

The dielectric constant of a slab of material through which a EM wave is allowed to propagate can be calculated according to equation 7, see [21]. This technique uses the phase derivative as a function of frequency to determine the dielectric constant, ϵ_r, of the material under test. In section 3.2.5 the theoretical background as well as a more detailed description is given,

however it can be concluded that if a 200 μm thick sample with a dielectric contrast variation of $\Delta\epsilon = 0.2$ the phase derivative will be as small as $0.1°/GHz$.

$$\epsilon = \left(\frac{\delta\phi}{\delta f} \cdot \frac{c}{360 \cdot d} + 1 \right)^2 \tag{7}$$

3.2 Theory concerning the constructed system

In this section the theory behind some of the key components and techniques used in the constructed system section 4. Some microwave technology will be presented together with a discussion about optics.

3.2.1 SSB up-converter

Here the operation principle of a SSB up-converter is described. The up-converter can be configured in two ways as shown in Figure 19 and Figure 20. The two setups operate as lower sideband, LSB, up-converter and upper sideband, USB up-converter respectively.

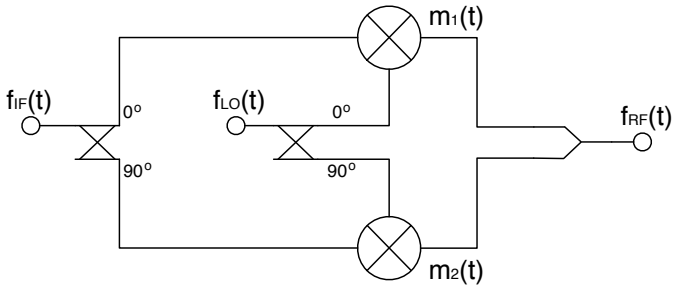

Figure 19: Schematic of LSB up-converter.

The operation of the LSB up-converter can be described as follows:

$$\begin{aligned} m_1(t) = cos(\omega_{LO} \cdot t) \cdot cos(\omega_{IF} \cdot t) = \\ = \frac{1}{2} cos(\omega_{LO} \cdot t - \omega_{IF} \cdot t) + \frac{1}{2} cos(\omega_{LO} \cdot t + \omega_{IF} \cdot t) \end{aligned} \tag{8}$$

$$\begin{aligned} m_2(t) = cos(\omega_{LO} \cdot t - \frac{\pi}{2}) \cdot cos(\omega_{IF} \cdot t - \frac{\pi}{2}) = \\ = \frac{1}{2} cos(\omega_{LO} \cdot t - \omega_{IF} \cdot t) - \frac{1}{2} cos(\omega_{LO} \cdot t + \omega_{IF} \cdot t) \end{aligned} \tag{9}$$

$$f_{RF}(t) = cos(\omega_{LO} \cdot t - \omega_{IF} \cdot t) \tag{10}$$

The difference between LSB and USB operation is the orientation of the IF hybrid. For LSB operation the LO and IF hybrids should be connected

with the in-phase outputs to one mixer and the quadrature outputs to the other. In the USB case the mixer that is connected to the in-phase LO is connected to the quadrature IF. The derivation of USB operation is done

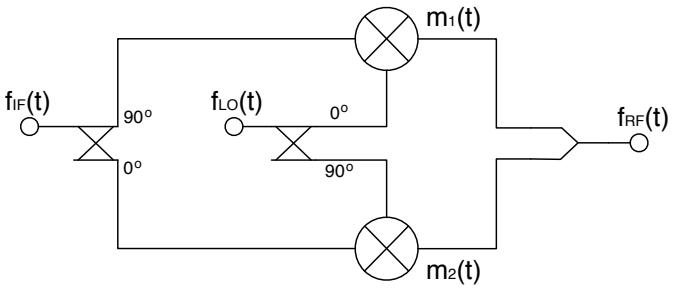

Figure 20: Schematic of USB up-converter.

below:

$$m_1(t) = cos(\omega_{LO} \cdot t) \cdot cos(\omega_{IF} \cdot t - \frac{\pi}{2}) = \\ = \frac{1}{2} sin(\omega_{LO} \cdot t + \omega_{IF} \cdot t) - \frac{1}{2} sin(\omega_{LO} \cdot t - \omega_{IF} \cdot t) \quad (11)$$

$$m_2(t) = cos(\omega_{LO} \cdot t - \frac{\pi}{2}) \cdot cos(\omega_{IF} \cdot t) = \\ = \frac{1}{2} sin(\omega_{LO} \cdot t - \omega_{IF} \cdot t) + \frac{1}{2} sin(\omega_{LO} \cdot t + \omega_{IF} \cdot t) \quad (12)$$

$$f_{RF}(t) = sin(\omega_{LO} \cdot t + \omega_{IF} \cdot t) \quad (13)$$

3.2.2 Quadrature demodulation

When two signals of the same frequency are fed to both the LO and RF port of a quadrature demodulator two DC voltages will appear on the in-phase and quadrature IF port respectively. Assuming that the LO port is fed with enough signal power a change in amplitude on the RF port will result in a change in the two DC output amplitudes. The I and Q signals can be considered to be the real and imaginary vector in the complex plane. Therefore the relative phase of the RF and LO signal as well as the amplitude of the RF signal can be acquired directly at the I and Q outputs.

3.2.3 IF reference to enable vector measurements

The ability to measure both the phase and amplitude of the received signal is critical for all imaging algorithms except simple power measurements where only the received power is considered. In order to measure the absolute phase a reference need to propagate through the measurement system. This

section will describe two different ways of achieving this in multiplier based measurement systems, to divide or multiply the reference. One other aspect that is important to remember is to have phase coherence in the system in order to cancel the phase noise of the microwave sources.

The first method described, the one used in the built system, is based on division and can be seen in Figure 21. The microwave source f_1 provides the signal to the LO multiplier chain which in turn creates the sub-millimetre wave LO drive, $n \cdot f_1$ to the mixer. A part of the f_1 signal is extracted in the coupler and used as LO drive to the quadrature modulator. The quadrature modulator together with the $\frac{\pi}{2}$ power splitter acts as a single sideband, SSB, up-converter, described in section 3.2.1. The reference oscillator creates the desired output frequency f_{REF} which is available at one of the outputs. f_{REF} is also divided and by the same factor used in the multiplier chains and feed to the quadrature power splitter. The output from the SSB modulator will then be either $f_1 + f_{REF}/n$ or $f_1 - f_{REF}/n$ depending on the IF hybrid orientation. After propagation through the transmit multiplier chain the the transmitted signal signal will be $n \cdot f_1 + f_{REF}$ or $n \cdot f_1 - f_{REF}$. Downconversion of the received signal will yield a IF frequency of f_{REF}. By comparing the SIG output with the REF output the received amplitude and phase can be extracted, see section 3.2.2 for an example. If the downconverter is operated using $f_{LO} < f_{RF}$ no spectrum inversion will occur. Another system operating by this principle can be found in [13].

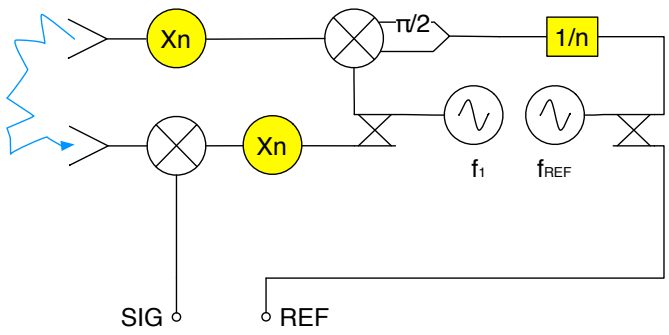

Figure 21: System block diagram where a divider is used to enable phase measurements.

An other way of solving the same problem can be seen in Figure 22. The technique has been used in [21] and [12] but was probably first described in [22]. The first source feeds a signal with frequency f_1 to the transmit multiplier chain giving a transmitted frequency of $n \cdot f_1$. The second source feeds a different frequency f_2 through the receive multiplier chain giving a LO frequency of $n \cdot f_2$. The resulting IF on the sub-millimetre wave mixer output will thus be $n \cdot |f_1 - f_2|$. The reference signal is created by mixing f_1

with f_2 and thereby creating $|f_1 - f_2|$. The mixer output is then multiplied by the same multiplication factor used in the other multiplier chains giving a REF output of $n \cdot |f_1 - f_2|$, the same as SIG. The mixing of the two sources might seem unnecessary to create the reference frequency but is absolutely necessary to achieve phase coherence through the system. If a third source was used as a reference instead it would not be phase locked on the output signal SIG.

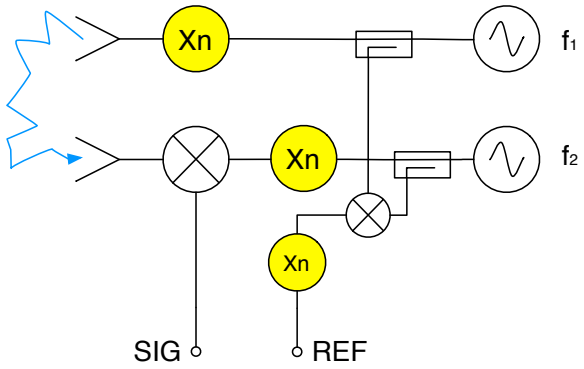

Figure 22: System block diagram where a multiplier is used to enable phase measurements.

It is also possible to use the SSB up-conversion together with the multiplication method, illustrated in Figure 23.

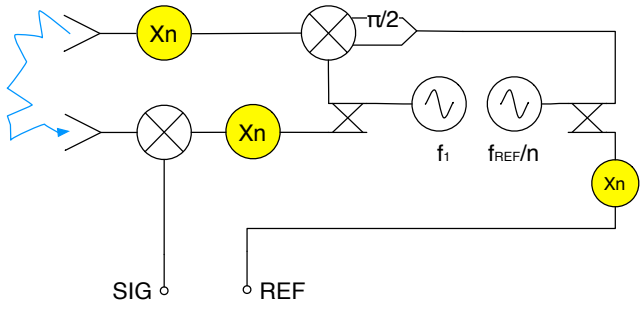

Figure 23: System block diagram where a multiplier and a SSB up-converter is used to enable phase measurements.

In all the systems described above phase coherence is achieved thus cancelling the phase noise of the microwave sources.

3.2.4 Optics

This section will describe the different optical approaches considered during the project. First some diffraction limited approaches and then two examples enabling sub wavelength imaging. A simple explanation of the diffraction limitation is that features in the imaged object smaller than λ, λ being the wavelength of EM wave, can not be resolved at imaging distances greater than λ.

First a catadioptric lens designed for operation at 108 GHz was evaluated. A description of the lens can be found in [23]. Measurements presented in section 5.1.4 concluded that a new lens needs to be produced for operation at 340 GHz.

Secondly a traditional quasi-optic approach using a Gaussian beam telescope was evaluated. The gaussian beam telescope can be described as two thin lenses separated by the sum of their focal distances. If the input beam waist is placed in the foci of the first lens the output beam waist will appear at the output foci magnified by the ratio of the lenses focal distance. One important aspect is that the setup is frequency independent. The design of such system is described in detail in [24], [25].

Finally it was decided that an image reconstruction algorithm originally developed for microwave tomography at a collaborating department will be used. Measurement data created with the aid of this project will later be used for image reconstruction. The algorithm is of the full non linear inversion type and uses a newton type algorithm to solve the non linear optimisation problem. A detailed description of the algorithm is beyond the scope of this work but the requirements it put on the system will be described.

If a well known receive and transmit antenna are placed facing each other the electromagnetic field solution between the antennas can be modelled with great accuracy. If a dielectric object then is placed between the antennas it will act as a scatterer of the EM radiation. If the antennas are moved in relation to each other while repeated measurements are performed the pertubated field solution, the field when the object is present, can be measured. By applying some non-linear integral solving techniques the properties of the dielectric scatterer can be estimated. More information about image reconstruction techniques can be found in [26].

This approach puts both mechanical and electrical demands on the measurement system. Firstly the shape of all objects in the imaging domain needs to be well known. The positioning of the receiver, transmitter and sample relative to each other needs to be known in the order of fractions of a wavelength, in this case approximately 10 μm since the wavelength is in the order of one millimetre. Finally the measurement accuracy and stability of the measurement of amplitude and phase must be within a few % and $^\circ$ respectively.

3.2.5 Determining ϵ_r by $\frac{\delta\phi}{\delta f}$

If an EM wave is allowed to propagate through a slab of dielectric material the phase will change at a different rate then if it was propagating through air since the wavelength differs as a function of ϵ. Measurements at multiple frequencies will give a phase derivative as a function of frequency. By modifying equation 7 the expected phase change per frequency can be calculated as shown in equation 14. As seen in Table 1 the phase derivative as a function of frequency, in $^\circ/GHz$, is relatively small for thin samples. For a sample 200 μm thick a dielectric contrast of $\Delta\epsilon = 0.2$ results in a phase derivative of only $0.1^\circ/GHz$. To determine such contrast the measurement equipment need to have a large bandwidth and good accuracy for relative phase measurements.

$$\frac{\delta\phi}{\delta f} = \frac{(\sqrt{\epsilon} - 1) \cdot 360 \cdot d}{c} \tag{14}$$

$\epsilon \backslash d[mm]$	**0.02**	**0.2**	**2**	**20**
1	0	0	0	0
2	0.0099	0.0994	0.9941	9.9411
2.1	0.0108	0.1078	1.0779	10.7793
2.2	0.01168	0.11598	1.1598	11.5978
3	0.0176	0.1757	1.7569	17.5692
5	0.0297	0.2967	2.9666	29.6656
10	0.0519	0.5190	5.1895	51.8947

Table 1: $\frac{\delta\phi}{\delta f}$ in $^\circ/GHz$ as a function of slab thickness and dielectric constant.

4 Construction of imaging system

In this section the development of the measurement system will be presented starting from the preceding 100 GHz scalar system and continuing with the development off two versions of the current 340 GHz vector measurement system. An intermediate 340 GHz scalar setup is also included. The design of the mechanical components including antenna fixtures and various mounting details are briefly described. The chosen focusing method is also presented.

4.1 Preceding 108 GHz scalar system

A previously constructed system serve as the basis of this work. The system was built with a $X3$ HBV multiplier as signal source and used an Ericson PM4 calorimeter as receiver, the system is reproduced in Figure 24 and presented in [23].

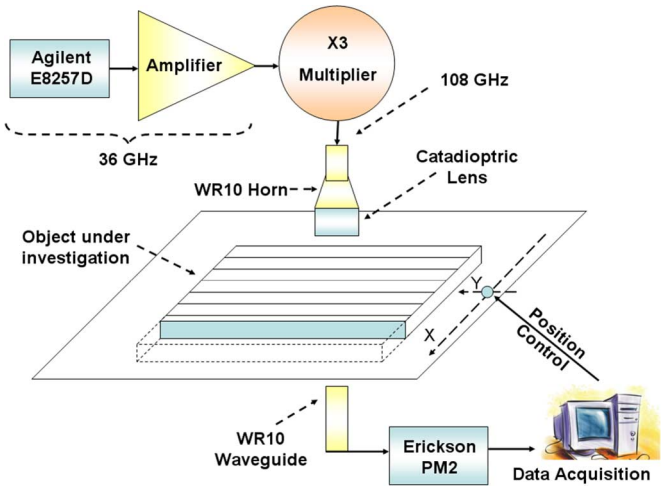

Figure 24: Preceding 108 GHz scalar system [23].

The focus was achieved by the combination of the catadioptric lens and the receive waveguide probe. Raster scanning of the sample was achieved by mounting the sample to a computer controlled mechanical stage and thereby moving it in the plane between the transmitter and receiver. The large drawbacks with this approach is the long time constant of the calorimeter, in the order of seconds, and the lack of phase information in the received signal.

4.2 Scalar 340 GHz system

As an intermediate step in the construction of the vector measurement system a scalar 340 GHz system was constructed. It uses the same sub-millimetre wave components as the final systems in section 4.3 and 4.4. As receiver a room temperature subharmonic Schottky mixer was used, the received signal was detected by a commercial microwave power meter. The mixer LO drive signal was provided by a HBV quintupler fed by a microwave synthesiser and a power amplifier. The illumination signal was in turn created by a chain of Schottky multipliers and amplifiers. The specific receiver used is described in [27] and a more general summary of THz sources can be found in [28]. The System is reproduced in Figure 25.

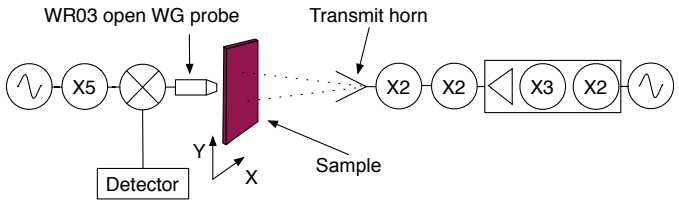

Figure 25: Scalar 340 GHz imaging system

The same mechanical stage as described in section 4.1 was used for moving the sample. A picture of the complete setup is shown in Figure 26.

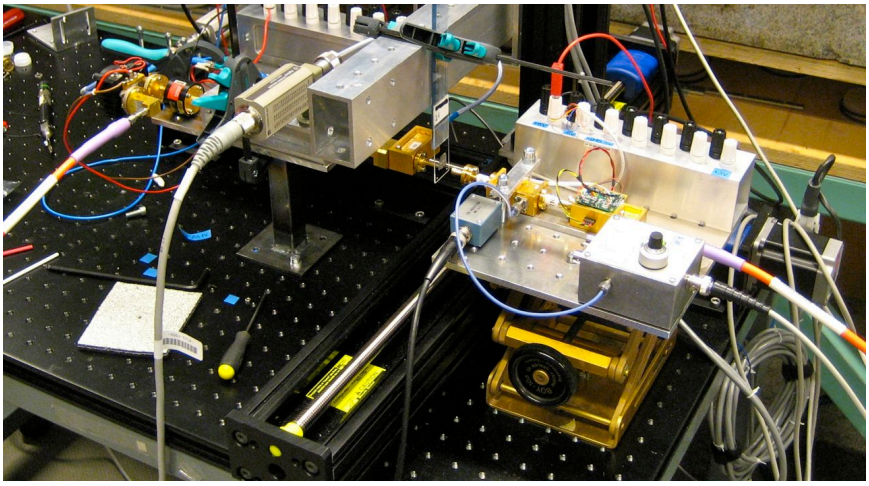

Figure 26: Picture of the measurement setup including the mechanical stage.

4.3 Schottky based 340 GHz vector measurement system

To compare different multiplier technologies two measurement systems were constructed, one using Schottky and one using HBV millimetre wave multi-

pliers. It should be noted that other multiplier technologies are used at the lower frequencies in the system. This section presents the Schottky version and the HBV based solution can be found in section 4.4.

The system block diagram, shown in Figure 27, reveals that the sub-millimetre wave multiplier chains used are the same as in the transmitter in the scalar system. This time however two identical chains are used and combined with the subharmonic mixer and the $X2$ transmit multiplier the multiplication factor becomes $X24$ in both chains. If the multiplication factor differs between the transmit and receive chain the IF frequency will not be the same as the reference.

The IF chain is the part that differs most form the scalar setup. It consists of a SSB up-converter, described in section 4.3.3, a frequency divider, section 4.3.2, a quadrature demodulator, section 4.3.1, and some amplifiers and filters. To enable phase and amplitude measurements the method with a divided reference frequency described in section 3.2.3 is used.

After the first downconversion in the sub-harmonic Schottky mixer a second downconversion is performed in the quadrature demodulator, described in section 4.3.1, the signal is then amplified and finally detected by two bench top multimeters.

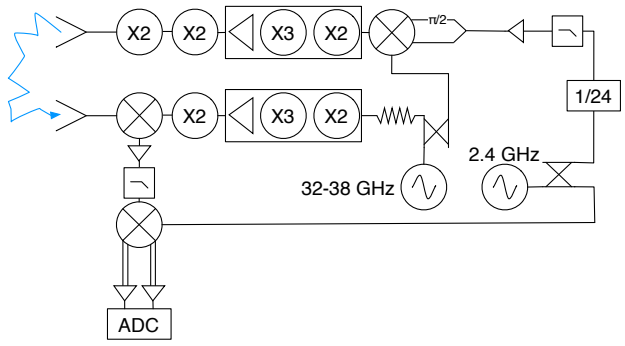

Figure 27: Schottky based 340 GHz vector measurement system.

The details regarding some of the system components are described in the sections below.

4.3.1 Quadrature demodulator

The quadrature demodulator circuit is realised according to the block diagram in Figure 28. An evaluation board for Analog Devises AD5382 quadrature demodulator is used together with two evaluation boards for the differential to single ended instrumentation amplifier AD 620. The operation principle of the downconverter is further described in section 3.2.2 but the conclusion is that the in-phase and quadrature output DC voltages represent

the X and Y vectors in the phase and amplitude plane of the received signal. The outputs from the instrumentation amplifiers are captured by two bench top multimeters through a Matlab script.

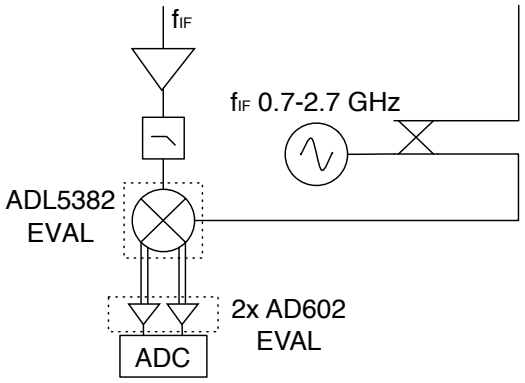

Figure 28: Schematic of the quadrature downconverter, amplifiers and ADC.

4.3.2 Frequency divider

As described in section 3.2.3 a frequency divider is needed in order to allow the phase reference to propagate throughout the system. This is solved by using a custom designed frequency divider circuitry.

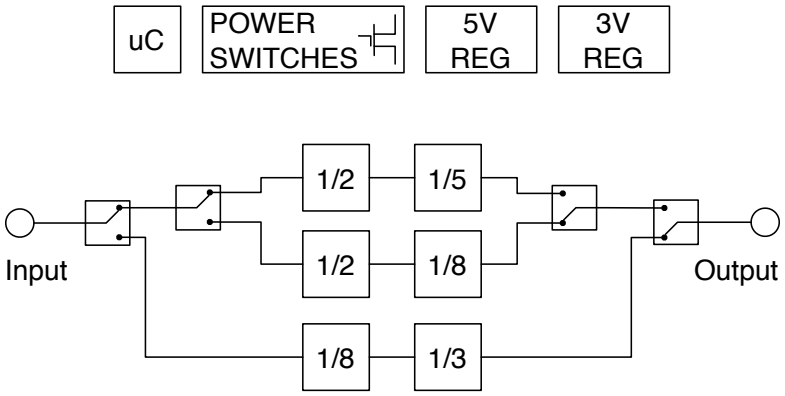

Figure 29: Block diagram of divider circuit

In order to provide flexibility to enable the use off different millimetre wave equipment the division ratio can be switched between three different

values, in the current configuration the available division ratios are, 10, 16 and 24. The values are in turn determined by the components used to populate the circuit board. The circuit is broadband with an operating frequency range of approximately $0.001 - 3\,GHz$. The frequency division circuits work as digital counters, thus resulting in a square wave output. As a result of the large bandwidth an external low-pass filter adapted to the specific output frequency and division ratio is required. Three different paths through the circuit can be selected as indicated in Figure 29. GaAs MMIC SPDT switches are used to control the signal path. To avoid interference between the division circuits only those in operation are connected to the supply voltage. The power switching is achieved using MOSFET switches. Both power and signal switches are controlled by an on board micro-controller. A photograph of the circuit is shown in Figure 30.

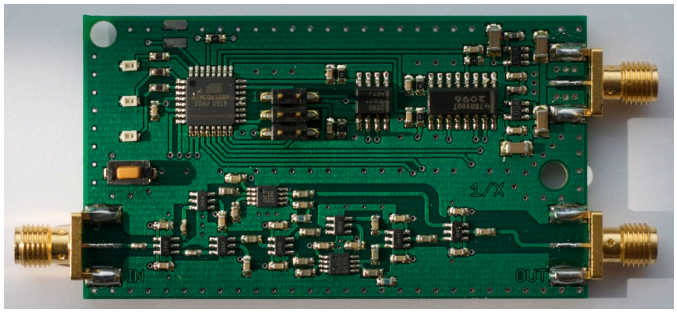

Figure 30: Photograph of the constructed frequency divider circuit.

4.3.3 SSB up-converter

The SSB up-converter, theory is described in section 3.2.1, is realised in two versions since the operating frequency differs between the Schottky and HBV based vector measurement systems. The IF $\pi/2$ phase splitter got a bandwidth of $80 - 120\,MHz$ and is used in both configurations. To cover a system operating frequency of $320 - 380\,GHz$ the SSB up-converter needs a RF output bandwidth of $13.3 - 15.8\,GHz$ or $32 - 38\,GHz$ for the Schottky and HBV system respectively. The two mixers used and their key properties are listed below:

- Marki IQB-0618
- RF bandwidth: $6 - 18\,GHz$
- IF bandwidth: $DC - 5\,GHz$
- LO-RF isolation: $20\,dB$
- Image rejection: $20\,dB$

- Hittite HMC-C047
- RF bandwidth: $30 - 38\,GHz$
- IF bandwidth: $DC - 3.5\,GHz$
- LO-RF isolation: $35\,dB$
- Image rejection: $15\,dB$

Since both mixer are configured for quadrature operation they consist of two mixers and an LO hybrid integrated to one package. The most important parameters for the up-converter is the relative suppression of the LO to RF leakage and the sideband suppression. The reason for this is that since the IF frequency is small in relation to the RF frequency it is not possible to use filters to reject those unwanted signals.

4.4 HBV based 340 GHz vector measurement system

The main difference between the HBV system and the previously described system is that two $X5$ HBV quintupler multipliers are used as main multipliers, together with two input power amplifiers. This changes the total multiplication factor of the system as well as the microwave input frequency. Consequently the division ratio in the frequency divider needs to be changed. The SSB up-converter is also built around a different mixer since the operating frequency band is changed. The modified system is presented in Figure 31.

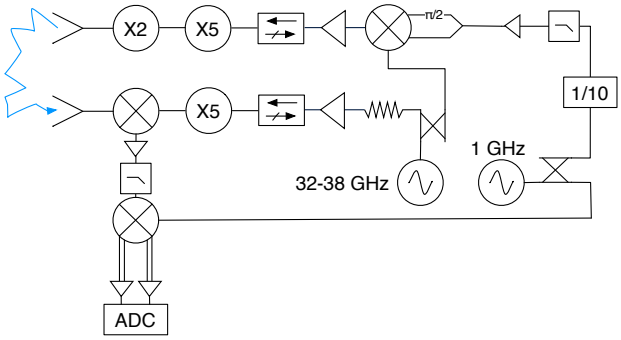

Figure 31: HBV based 340 GHz vector measurement system

4.5 Optics

This section describes some different optical approaches evaluated during the work.

4.5.1 Open waveguide probe.

A method used in some of the experimental test conducted during the project is the combination of an open waveguide probe and a horn. The open waveguide probe is placed on either the receiver or transmitter and the opening is placed within a few wavelengths from the sample while the horn is placed on the other module further away. By combining this with a raster scan step in the order of $\lambda/10$ or smaller an image resolution close to the diffraction limit can be achieved.

4.5.2 Gaussian telescope approach

A gaussian telescope approach, described in section 3.2.4 realised by two off-axis parabolic mirrors is the result of a more classical quasi-optical design study. By combining two parabolas with a focal distance ratio of $2:1$ the beam waist produced by the horn can be focused to a spot on the sample that is half of the horn beam waist. The choice of focal ration comes from the fact that the beam waist in the horn is approximately $2\,\lambda$ which gives a focused spot size at the diffraction limit. The design has not yet been realised.

4.5.3 Catadioptric lens

The feasibility of using the catadioptric lens, introduced in section 3.2.4 and used in the system in section 4.1, designed for operation at $108\,GHz$ in this system at $340\,GHz$ has been evaluated in section 5.1.4. It was found that the lens needs to be redesigned in order to operate in the $340\,GHz$ band.

4.5.4 Image reconstruction

The chosen solution for focusing is a full non linear inversion algorithm. The reason for using such algorithm is that it enables sub wavelength focusing with a long focal depth and also adds a degree of novelty to the system.

In order to enable the use of the image reconstruction algorithm described in section 3.2.4 it is necessary to be able to create an accurate electromagnetic model of the imaging region. This puts demands on the accuracy of which the position of all the components in the system is known as well as the exact physical shape of the objects. In order to keep computing time at realisable levels the imaging domain must be restricted to a volume of approximately $1000\,\lambda^3$. Furthermore the phase and amplitude measurement accuracy of the system must be kept to within a few percent.

After some evaluation of available horn antennas it was decided that a custom designed open waveguide probe shall be manufactured. One of the reasons is that the shape of the metallic parts inside the imaging region can

be accurately determined. The open waveguide probe is presented in section 4.6.2

A system that is believed to meet the mechanical requirements is presented in section 4.6.1 and assembly is currently ongoing.

4.6 Mechanical components

In this section mechanical components that has been constructed during the project will be presented.

4.6.1 4-axis mechanical setup

The imaging algorithm described in section 3.2.4 requires precise movement of the receiver and transmitter in two parallel planes with the sample placed in a plane in between. The realisation of this is done by extending and rebuilding the 3-axis mechanical stage used in the preceding system, section 4.1 with a fourth axis. The new configuration enables movement in two parallel planes as can be seen in Figure 32.

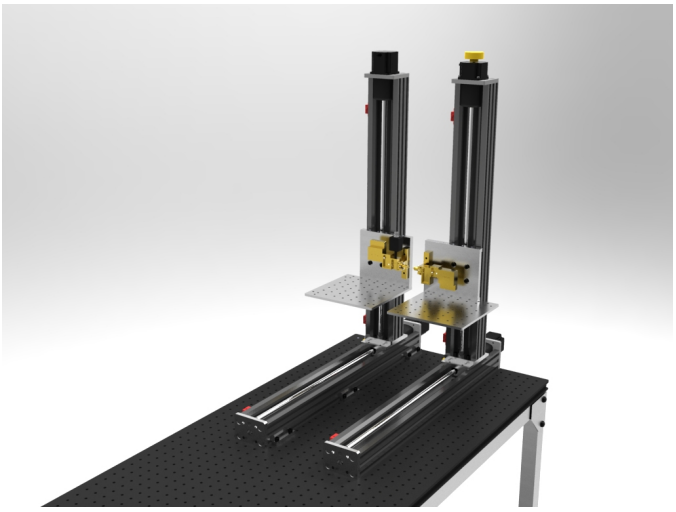

Figure 32: Over view of the mechanical setup.

A precise and repeatable mounting of the receiver is required an therefore an adapter was constructed that fixes the antenna to the mounting bracket of the moving axis. A study conducted showed that a custom designed waveguide probe was a suitable antenna since the directivity is relatively low. This means that the beam is wide and illuminates the whole imaging region simultaneously. However the antenna mounting is compatible with all horns using the standard UG-387 flange. A picture of the mounting assembly together with the multiplier chains is shown in Figure 33.

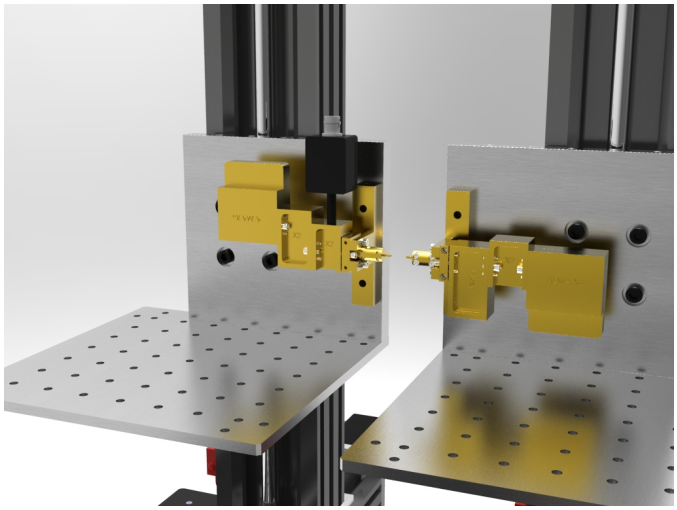

Figure 33: Antenna fixtures mounted on 4-axis stage, note that the imaging region is between the two probes.

4.6.2 Custom WR-2.8 waveguide probe

Figure 34 shows a rendering of the custom designed waveguide probe. The mechanically well defined probe is necessary to enable implementation of a complete *EM* model of the system.

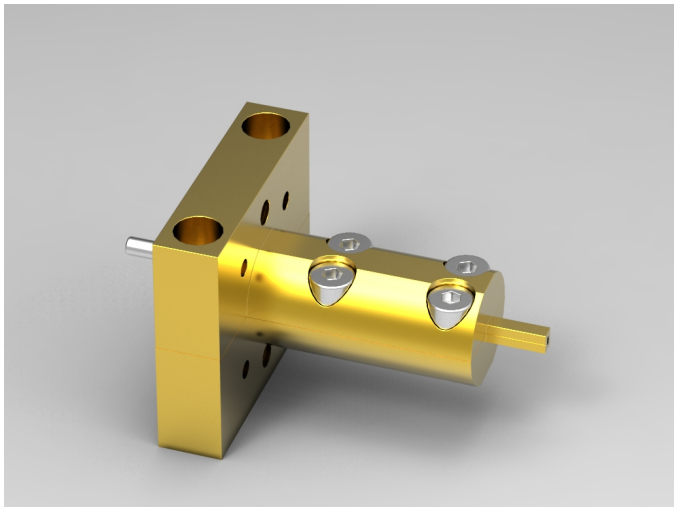

Figure 34: The constructed waveguide probe.

4.6.3 Divider PCB

As a part of the construction of the frequency divider circuit a printed circuit board was designed and ordered, se Figure 35. Drawings can be found in Appendix B.

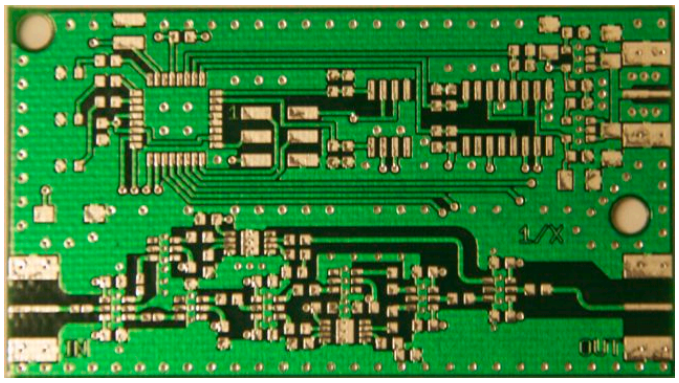

Figure 35: Unpopulated frequency divider PCB

4.6.4 Lens holder

In order to enable more accurate testing of the catadioptric lens a lens holder was manufactured, se Figure 36.

Figure 36: Lens holder with catadioptric lens.

4.6.5 Mounting plate

As part of the mechanical support setup optical breadboard like mounting plates with connectors for a number of supply voltages were manufactured, se Figure 37.

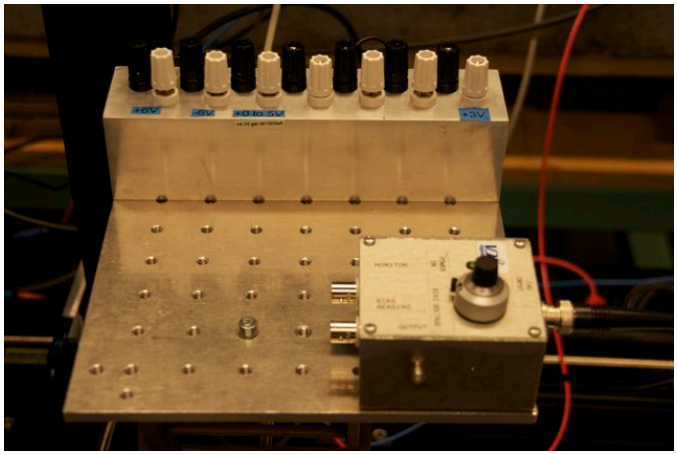

Figure 37: Mounting plate with thread pattern and power connections.

5 Measurements

This section will present different measurements that have been done.

5.1 System characterisation

In this section characterisation of different system components will be presented as well as measurements on various samples.

5.1.1 Characterisation of vector measurements

In this section measurements done in order to characterise the phase and amplitude measurement capabilities of the constructed system will be presented.

The following measurements were carried out with the system configuration shown in Figure 38. The transmitter and receiver are connected back to back using a piece of waveguide.

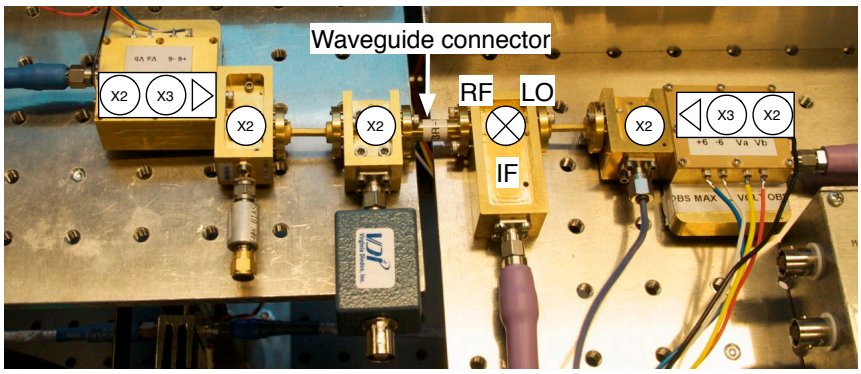

Figure 38: System connected back to back.

In order to set the boundaries of following measurements the available power at the CW source as well as output source multipliers was measured. The result from the CW source can be seen in Figure 39. It is apparent that output power is available in the approximate range $320 - 365\,GHz$. The LO multiplier delivers output power over a frequency range covering that of a the CW source, shown in Figure 40 where the effective LO frequency is used. However the mixer requires at least $3\,dBm$ of pump power thus the usable band will be narrower.

The final usable bandwidth is dependent of many parameters such as the matching bandwidth at different mixer ports and mixer conversion loss as

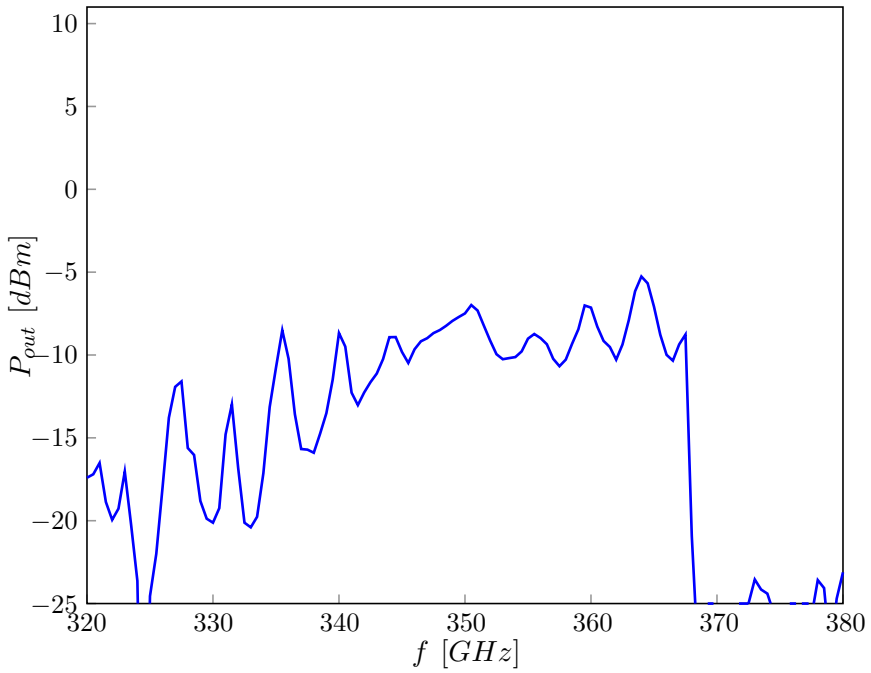

Figure 39: Output power from the CW signal source.

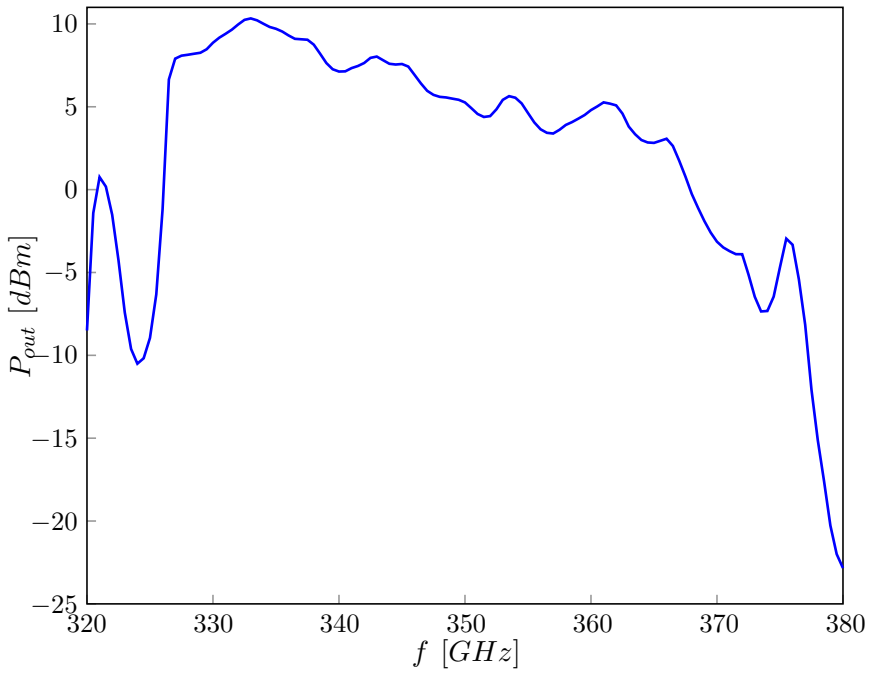

Figure 40: Output power from the LO multiplier, note that the effective LO frequency is plotted and that the real frequency is half of that.

a function of frequency. Using the system in Figure 38 the received power was measured as a function of frequency, shown in Figure 41 with arbitrary power unit. The usable band is $326-348.5\,GHz$ giving a relative bandwidth of 6.5 % calculated from the band centre.

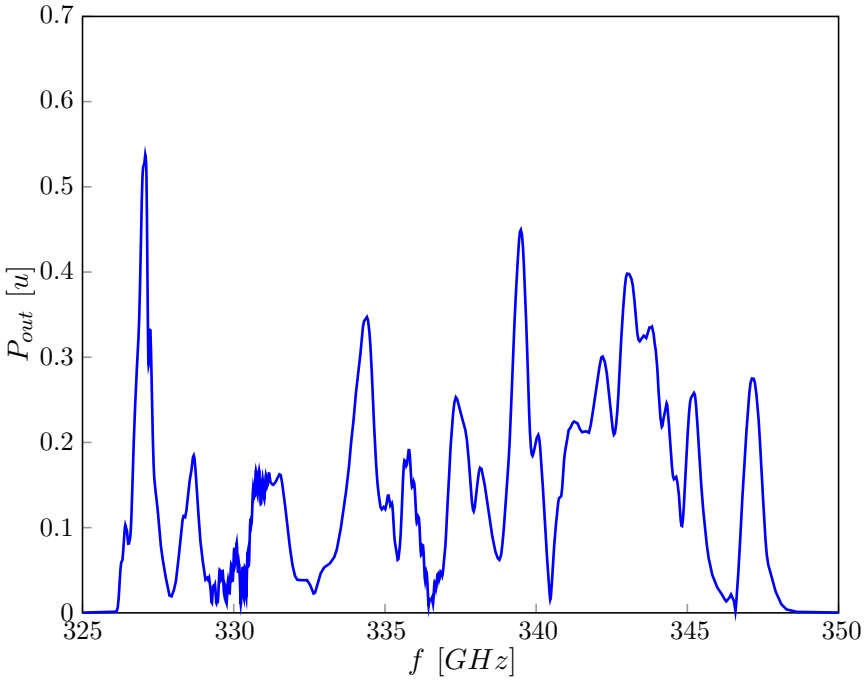

Figure 41: Received power as a function of frequency, arbitrary unit.

To characterise the repeatability of frequency swept measurements the frequency was swept repeatedly over the full bandwidth. The result is shown in Figure 42 and Figure 43 where amplitude and phase repeatability of two measurements close in time is presented.

The long term drift was evaluated both as the stability of a fixed frequency signal over time as well as the repeatability of a full swept measurement. The two measurements were conducted at different occasions. Figure 44 shows the fixed frequency measurement. As can be seen the maximum phase span is approximately 90°. By closer examination it can be seen that the phase slowly drifts within this region. The measurement time was approximately 12 hours. The frequency swept phase drift shows similar characteristics.

To visualise errors or unbalance in the phase and amplitude measurement over a full phase revolution the receiver was mounted on a movable stage and moved with 0.01 mm steps towards the transmitter. In this way the phase of the received signal will vary with a negligible change in amplitude. A principal sketch of the setup is shown in Figure 45.

The result of one test at 327 GHz is shown in Figure 46. The receiver

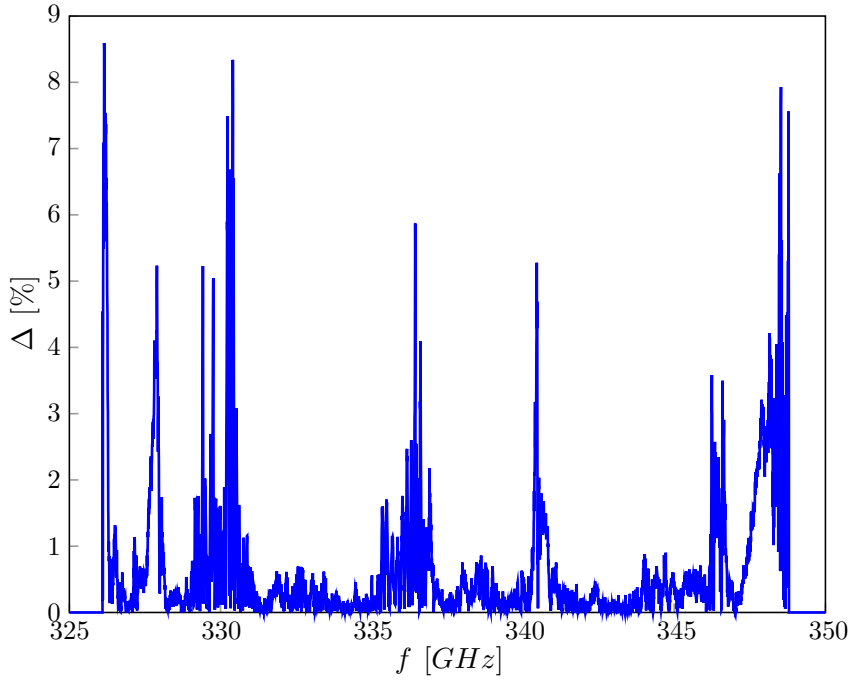

Figure 42: Short term amplitude measurement repeatability, high error occurs when the SNR decreases.

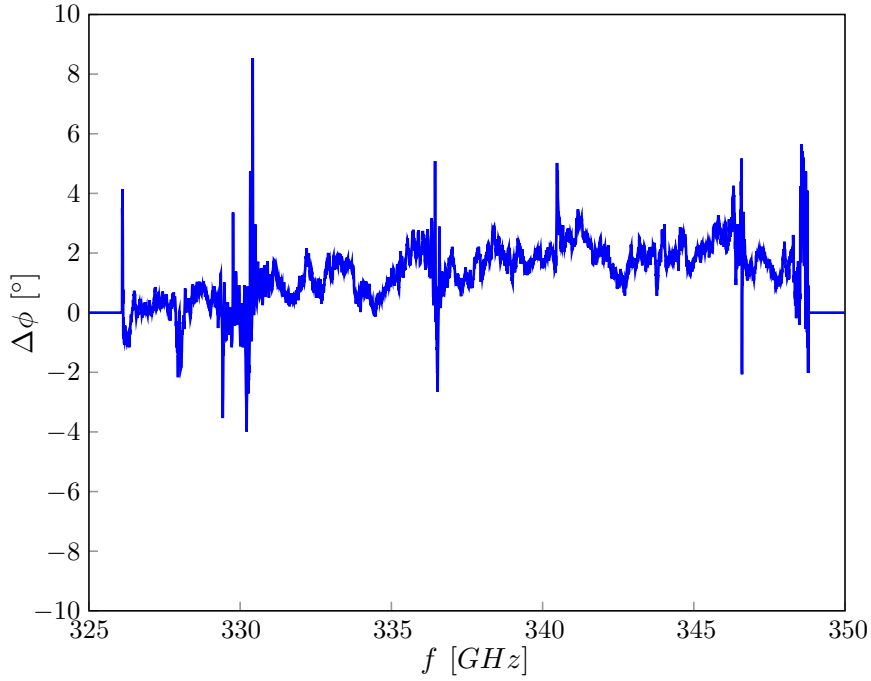

Figure 43: Short term phase measurement repeatability, high error occurs when the SNR decreases.

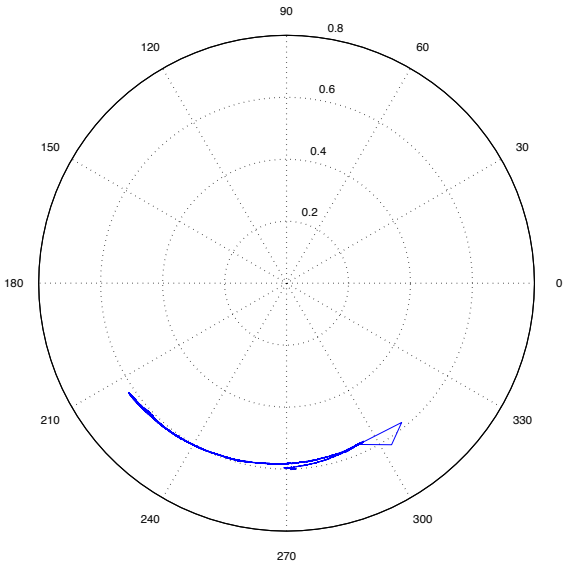

Figure 44: 12 h phase drift at fixed frequency.

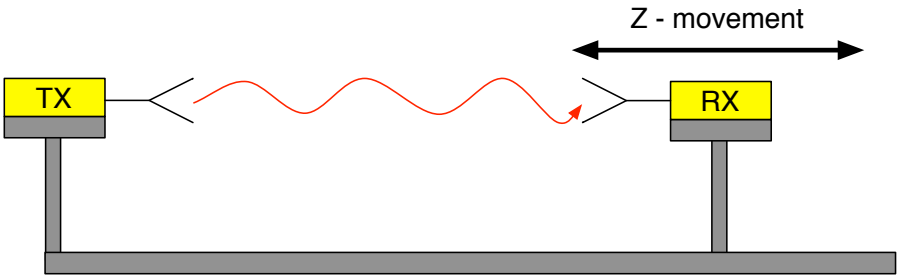

Figure 45: Sketch showing the principle behind the measurement.

is moved in $10\,\mu m$ steps over a total travel length of $2\,mm$. The symmetric unbalance is believed to come from standing waves in the system.

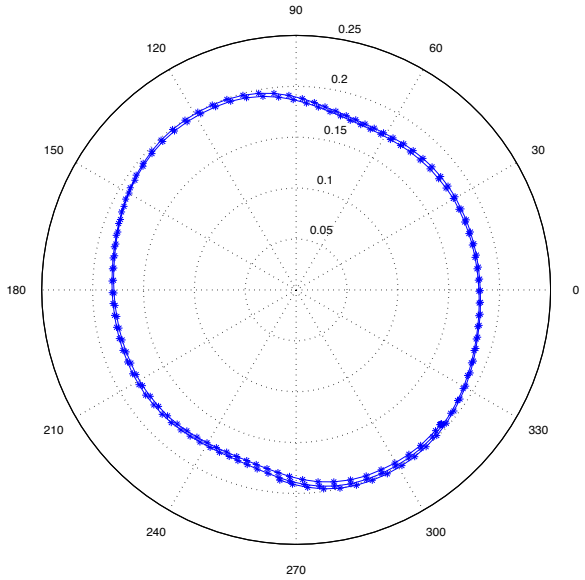

Figure 46: Measurement result from linear translation of the receiver in relation to the transmitter.

5.1.2 Frequency divider measurements

All three division ratios of the constructed frequency divider were tested with a $1\,GHz$ input signal. The three different ratios behaved similarly, the only difference being the choice of output filter which is depending on the output frequency. The unfiltered waveform of the divide by 10 configuration is shown in Figure 47 together with the filtered waveform in figure 48.

As seen in the overlaid FFT plot in Figure 48, the suppression of the harmonics is better than $20\,dB$.

5.1.3 30 GHz power amplifiers

In this section characterisation of the power amplifiers used to drive the HBV multipliers will be presented.

Spacek SP424-35-31W SN 6K08 In this section measurement results for the amplifier Spacek SP424-35-31W SN 6K08 will be presented. Figure 49 and 50 shows the output power and gain with the input power swept from $-15\,dBm$ to$-14\,dBm$. The figure suggest that the amplifier might be usable, i.e delivers $26\,dBm$, in the $33-36\,GHz$ range which equals $330-360\,GHz$ with a $X10$ multiplication factor.

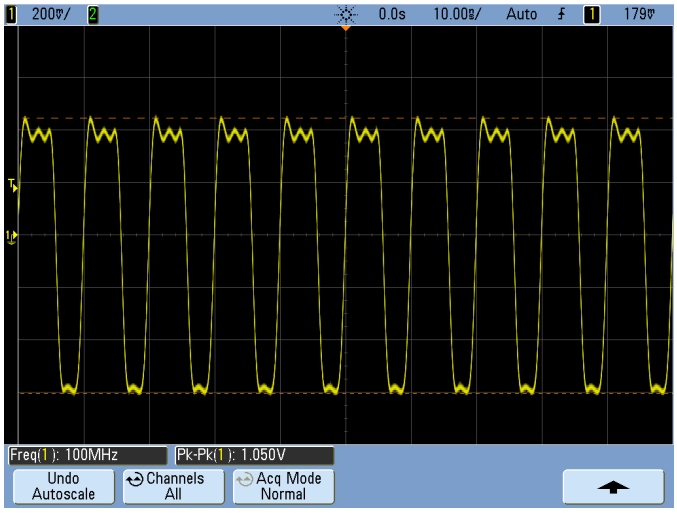

Figure 47: Unfiltered output waveform from the frequency divider set to 1/10 with a 1 GHz input.

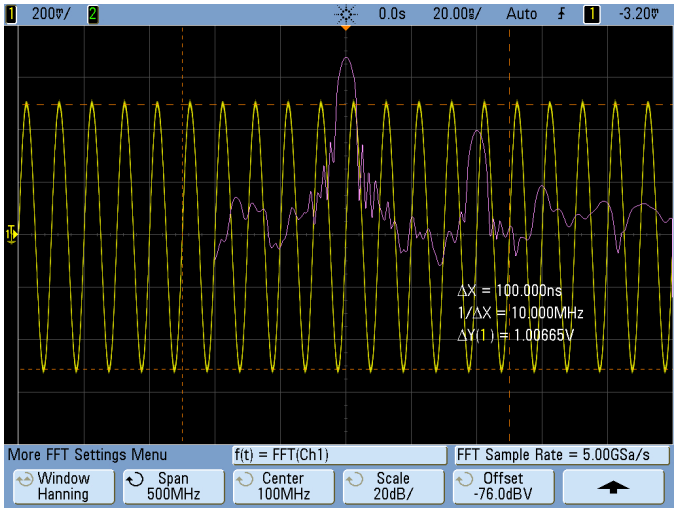

Figure 48: Filtered output waveform from the frequency divider set to 1/10 with a 1 GHz input.

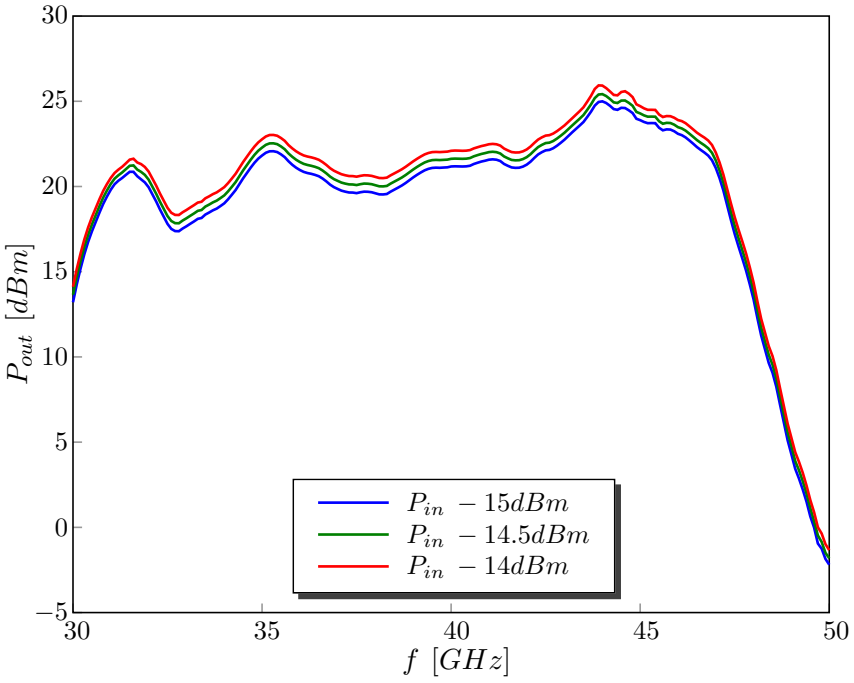

Figure 49: 6K08 output power.

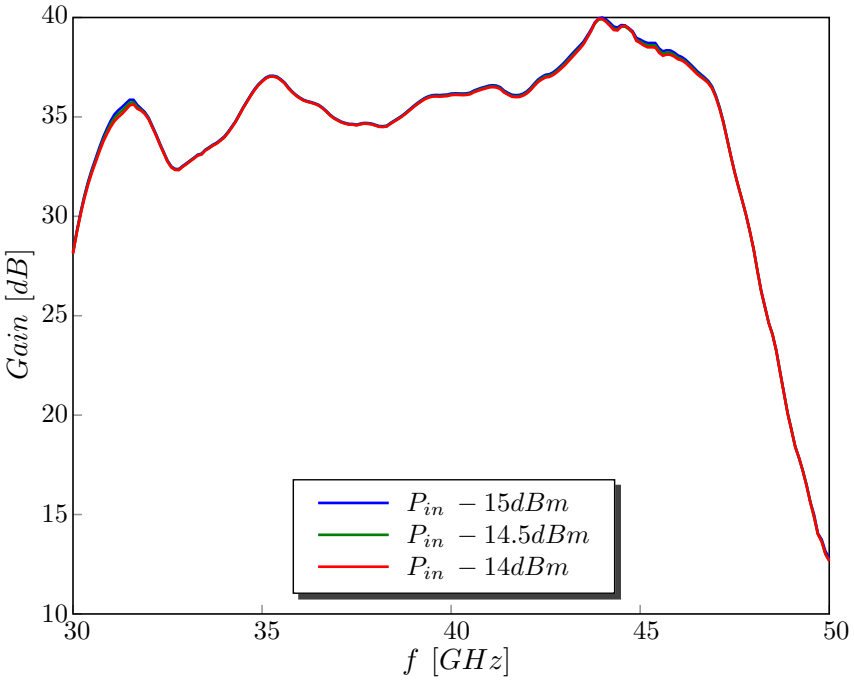

Figure 50: 6K08 gain.

To determine if the amplifier is usable as a multiplier pump source in the $33 - 36\,GHz$ range the output power was measured with the amplifier driven into saturation. Figure 51 and 52 shows saturated output power and gain.

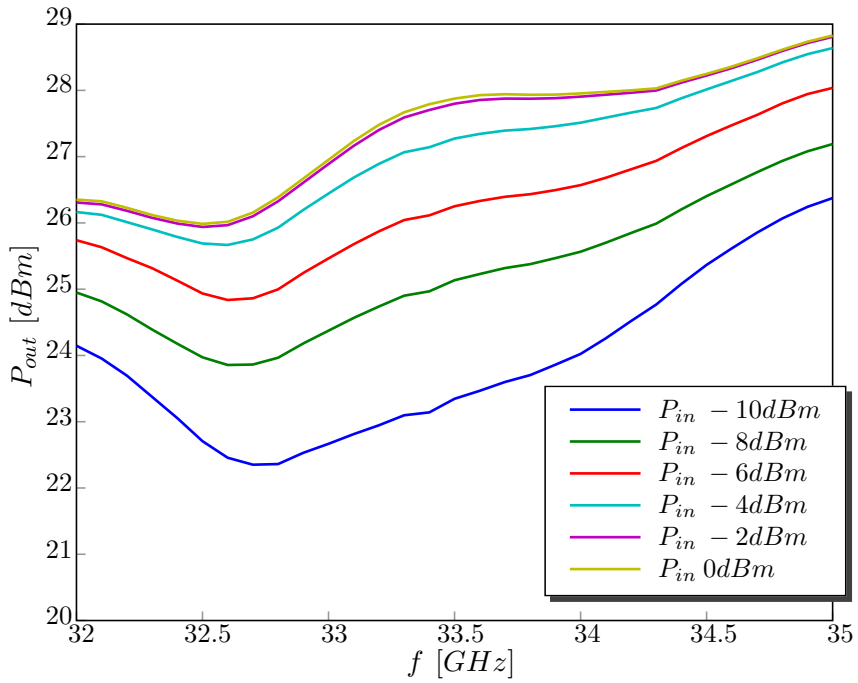

Figure 51: 6K08 narrow band saturated output power.

SP342-35-31W SN 5H16 In this section measurement results for the amplifier Spacek SP342-35-31W SN 5H16 will be presented. Figure 49 and 50 shows the output power and gain with the input power swept from $-10\,dBm$ to $0\,dBm$.

Spacek SP424-35-31W SN 6K08, HBV1 and VDI WR2.8x2 Here an output characterisation of a chain consisting of Spacek SP424-35-31W SN 6K08, HBV1 and VDI WR2.8x2 will be presented. The motivation for the measurement is to see whether it can be a valid alternative for the system transmit chain. The output power from the HBV, driven at $27\,dBm$, is on the limit of being to low. A higher input power to the VDI doubler is desirable. Figure 55 shows the output power of the chain, note that the BW is $335-358\,GHz$, i.e $6.6\,\%$ relative bandwidth calculated from the band centre. Figure 56 shows the amplifier gain at an output level of $27dBm$.

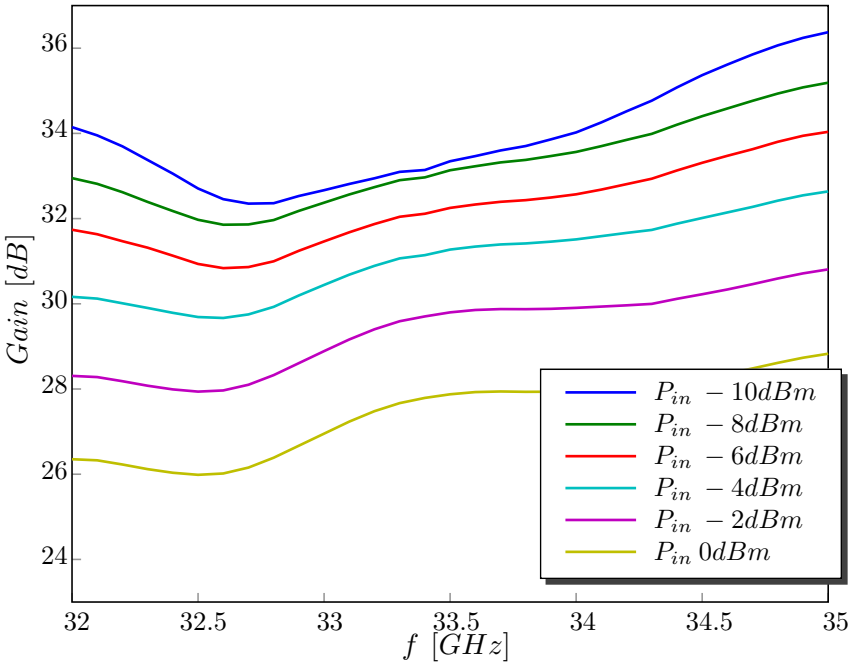

Figure 52: 6K08 saturated gain.

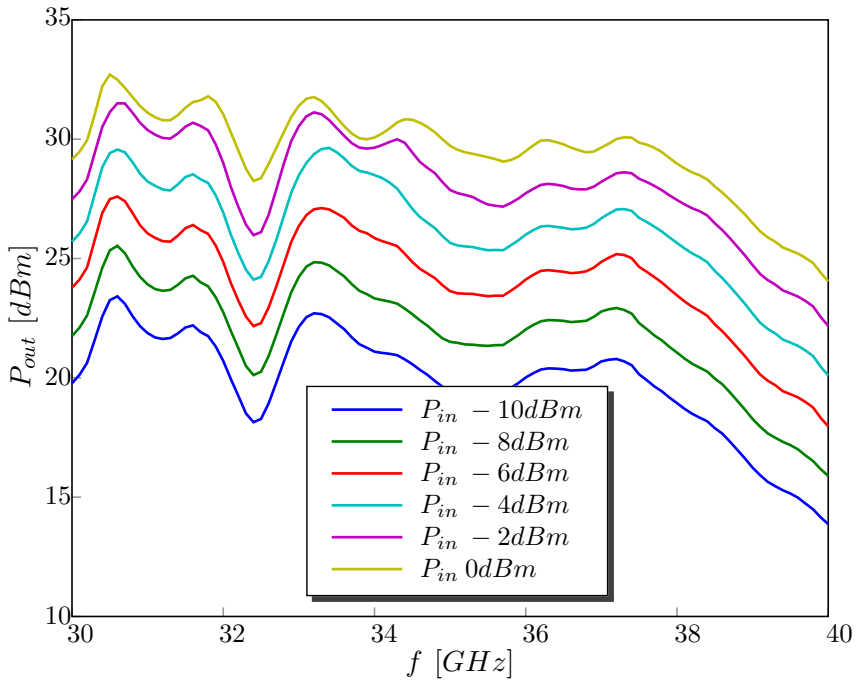

Figure 53: 5H16 output power.

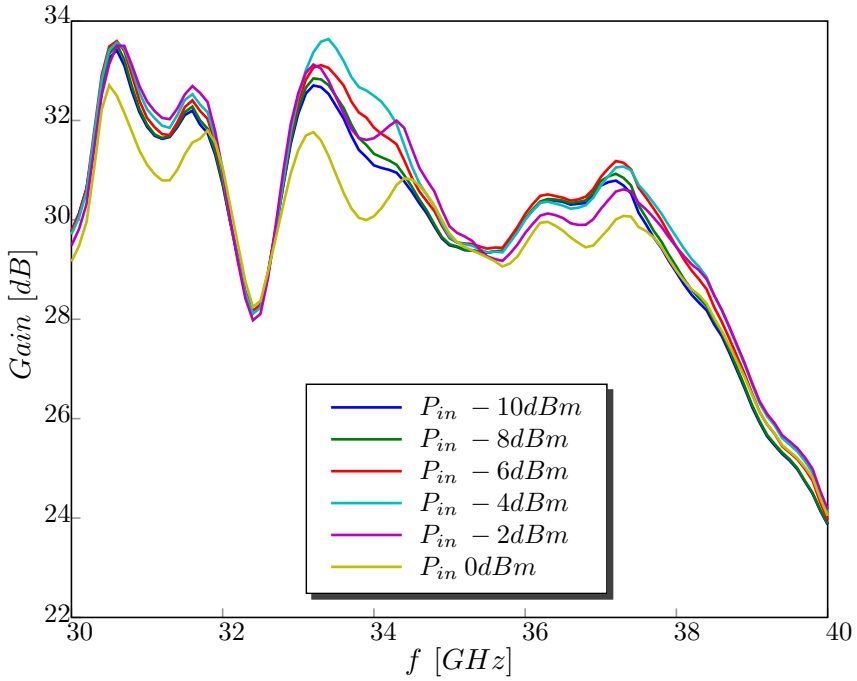

Figure 54: 5H16 gain.

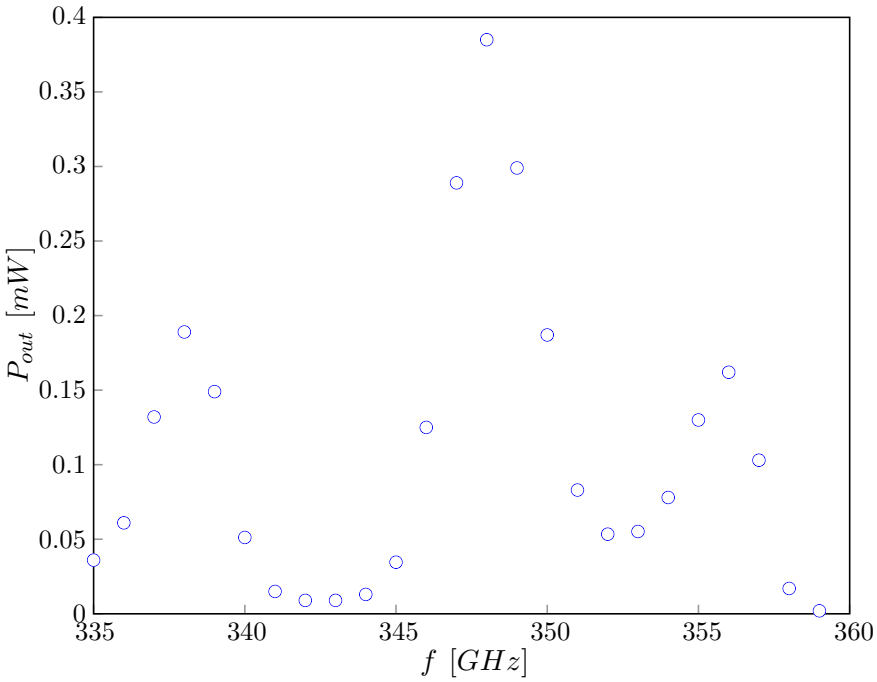

Figure 55: 6K08, HBV1 and VDI WR2.8x2 output power, frequency is at the final multiplier output.

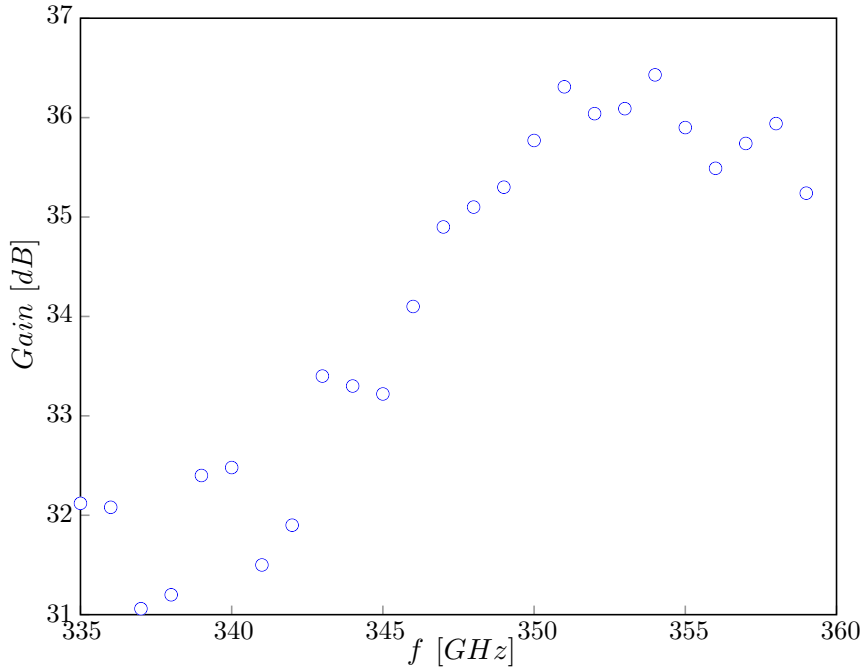

Figure 56: 6K08 amplifier gain plotted for the constant output power of 27 dBm used, frequency is at the final multiplier output.

5.1.4 Characterisation of catadioptric lens at 340 GHz

The catadioptric lens is further described in [23]. For this setup a lens originally constructed for use at 108 GHz is used. This section will present the characterisation results of the same lens at 333 GHz. One method used to characterise the lens is field probing using an open waveguide. The field probing revealed that the loss in the lens was approximately 20 dB. Additionally WR-03 vector network analyser extenders were used to find the return loss of the lens. The return loss from the horn without the lens mounted was better than 20 dB and when the lens was mounted the return loss degraded to $10 - 15\,dB$

5.1.5 SSB Up-conversion

In this chapter the results from the single sideband up-conversion measurements are presented. As can be seen i Figure 57 the measurement setup consists of two signal sources, one $10 - 40\,GHz$ hybrid, one $80 - 120\,MHz$ quadrature power splitter, one I/Q mixer, a spectrum analyser and some cables. The mixer, Hittite HMC-C047, is specified at 17 dBm LO power, however the maximum output from the signal generator is 17 dBm at 33.5 GHz. Due to the power loss in the connecting cables and the hybrid, which is used

in the complete system described in section 4.4, the LO drive level is only $10 - 11\ dBm$. However this proved to be sufficient to produce an acceptable result, i.e approximately $20dB$ rejection of both LO and the unwanted sideband.

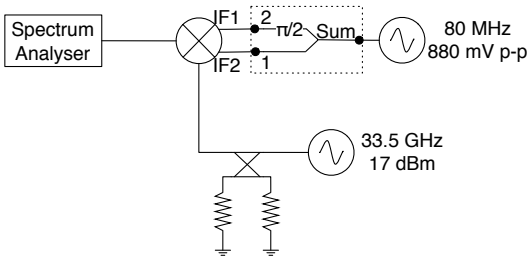

Figure 57: Measurement setup for sideband rejection test.

The result from the described measurement is shown i Figure 58 as an output spectrum plot and key data is summarised below.

- RF-LO 21 dB
- Sideband rejection 24.5 dB

By reversing the connections of the quadrature power splitter, connecting power splitter port 1 to mixer IF1 and power splitter port 2 to mixer IF2, the upper sideband will be rejected. The theory is explained in section 5.1.5. The output power spectrum is shown in Figure 59 and key data are summarised below.

- RF-LO 21 dB
- Sideband rejection 19 dB

To test the influence of the lack of LO power the hybrid was disconnected and the mixer connected directly to the signal generator using a short cable, the LO power increased to approximately 14 dBm. As seen below the performance degraded with the increase in LO power.

- RF-LO 19 dB
- Sideband rejection 17.5 dB

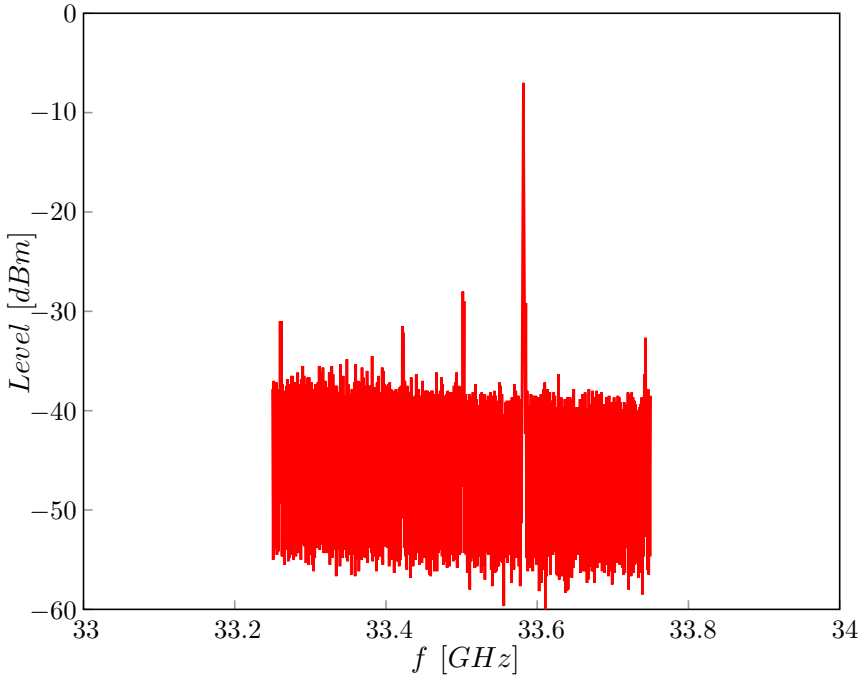

Figure 58: Test using upper sideband.

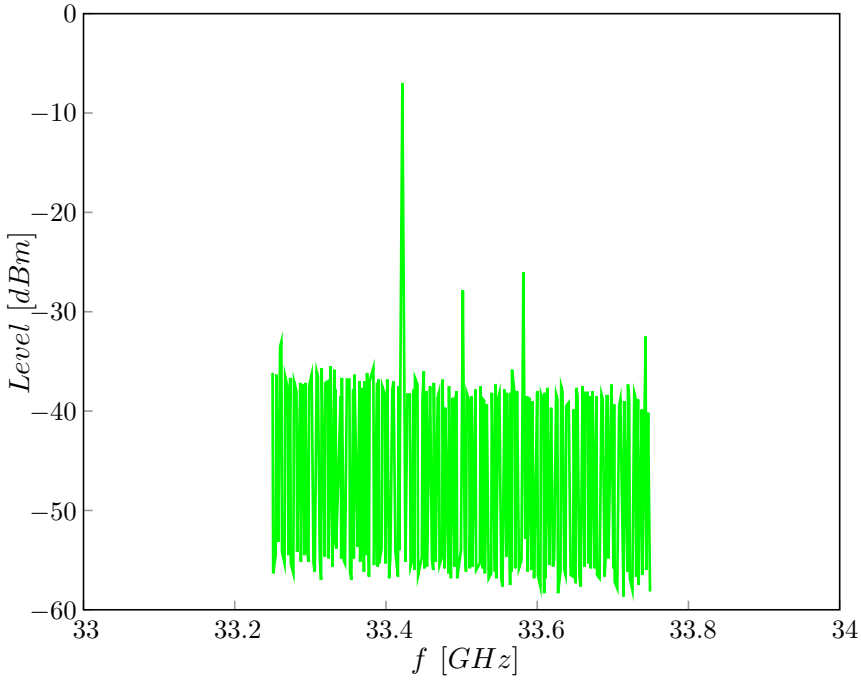

Figure 59: Test using lower sideband.

5.1.6 Quadrature demodulator

In this section the characterisation of the Analog Devices ADL8253 quadrature demodulator and the Analog Devices AD620 differential amplifiers are presented. The measurement setup is shown in Figure 60. The setup consists of evaluation boards for the quadrature demodulator and the amplifiers, two signal generators and two bench top multimeters. The two sources where linked together by a $10\,MHz$ reference and the variable phase shift was produced by changing the relative phase in one of the sources. A Matlab script was used to control the sources and collect the data. 360 data points were collected during approximately six minutes. The theory behind quadrature demodulation of two signals of the same frequency is described in section 3.2.2.

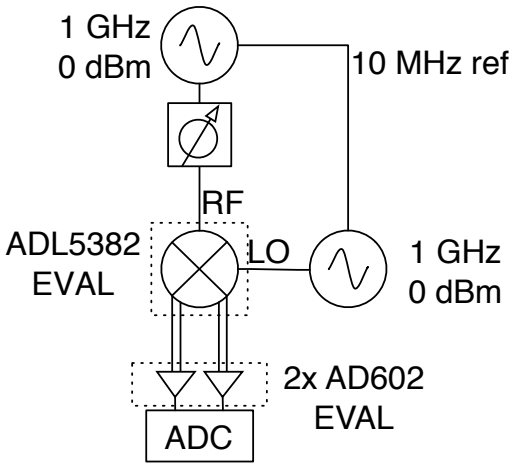

Figure 60: Measurement setup for characterisation of quadrature demodulator.

Before the setup if Figure 60 was tested the stability of the demodulator circuit and the influence of cable bends was evaluated. In the test only one signal source was used and the signal split by a quadrature hybrid was fed to both RF and LO inputs. In the first test the system was left resting on a table while 360 data points were collected during six minutes. The result is listed below, amplitude deviation is the difference between the smallest and largest amplitude recorded and angular deviation the difference between the smallest and largest angle recorded.

- Amplitude deviation 0.12 %
- Angular deviation 0.03°

The influence of cable bends was also evaluated by repeating the previous measurement but this time bend the connecting cable repeatedly during

the measurement. As the result below indicate both amplitude and phase deviation increased.

- Amplitude deviation 0.42 %
- Angular deviation 0.86°

Using the setup shown in Figure 60 the stability of the relative phase of the two sources was tested by collecting 360 data points during a six minute measurement. As can be seen in the result below and in Figure 61 the relative phase varies between measurements as well as drifts over time. This is probably due to the internal phase locking in the synthesisers.

- Amplitude deviation 0.16 %
- Angular deviation 2.40°
- Start to end angular deviation 1.62°

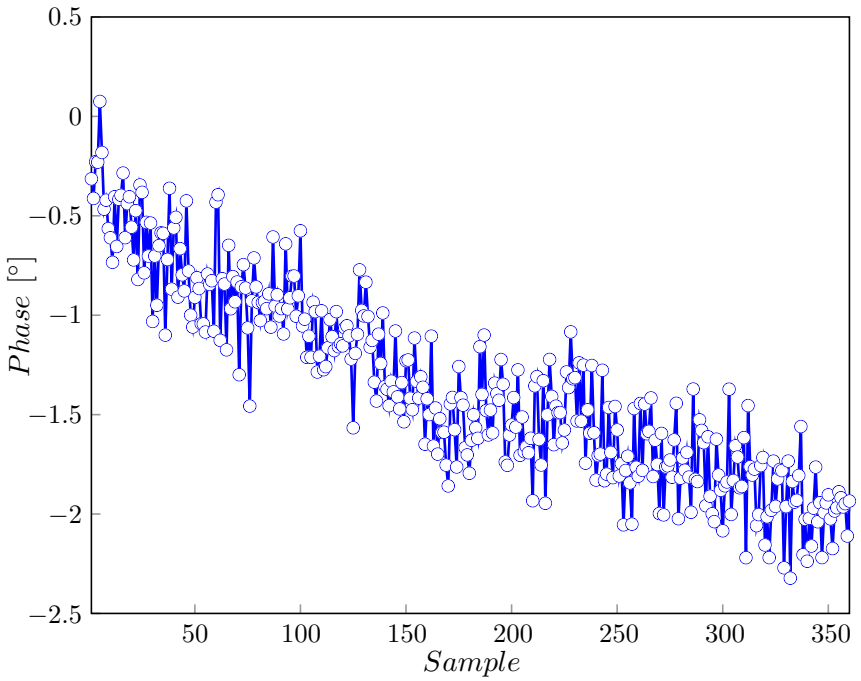

Figure 61: Phase drift during measurement

To test how the system reproduces different relative phases one of the synthesisers was set to advance its phase by 1° between every measurement. Both *LO* and *RF* level was 0 *dBm*. 360 data points were recorded corresponding to a full phase revolution. The test was repeated four times and

it turned out that the synthesiser changing its phase always ended up lagging approximately 10° after a full phase revolution. Since the accuracy of the input phase is unknown it is hard to estimate the absolute error of the measured phase. Some indication is however given in the amplitude stability which is approximately 2 % since the phase is calculated from the two amplitude vectors. The measurement data is shown in Table 2

Test	Amplitude deviation	Start to end angular deviation
1	2.2 %	8.1°
2	2.1 %	8.5°
3	2.4 %	10.7°
4	2.5 %	8.0°

Table 2: Results from the four measurements.

To investigate the effect of a change in RF power the same test was repeated with a RF power of $-20\,dBm$. As shown below the amplitude deviation increased significantly. From the measurement data the conclusion can be drawn that the centre of the circle created in the imaginary plane offsets from the real centre, therefore the large amplitude deviation.

- Amplitude deviation 15.9 %
- Start to end angular deviation 8.9°

6 Results

In this section results from measurements as well as construction tasks will be discussed and evaluated.

6.1 Performance of measurement system

This section will describe the result from the measurements aiming to characterises the performance of the sub-millimetre vector measurement system.

6.1.1 Amplitude and phase measurement accuracy

The parameters important in judging the performance of the vector measurements are mainly the measurement repeatability and drift. An error in absolute phase or amplitude will not necessarily degrade the performance of the imaging system if the error is repeatable and therefore can be compensated in software. As found in section 5.1.1 the repeatability between two measurements with a short separation in time is typically within 2° in phase and 1 % in amplitude.

As the measurement time is extended to several hours a larger drift can be seen.

When the horns were moved in a straight line in relation to each other a symmetric pattern can be seen in the measured phase and amplitude. Ideally the measured circle should be completely round and centred in the plane. The symmetric non ideal shape of the result is probably due to standing waves between the horns and it is therefore hard to judge the absolute accuracy of the system. It is however believed that the system stability is sufficient to satisfy the demands set by the image reconstruction algorithm. This assumption is based on the fact that short term repeatability is good and therefore a zeroing routine can be built into the software to compensate for the slow long term phase drift.

6.1.2 SSB up-converter

The measurements of the $30\,GHz$ version of the SSB up-converter evaluated in section 5.1.5 showed that the $RF - LO$ rejection as well as sideband rejection was good enough to not cause problems in the measurement system. An exact estimation of the suppression needed is hard to give but the system is relatively insensitive to unwanted harmonics due to the superheterodyne detection method.

6.1.3 Quadrature demodulator

The evaluation of the quadrature demodulator and the instrumentation amplifiers showed a good stability and accuracy. Since there were some prob-

lems with the phase locking of the sources the absolute measurement accuracy could not be determined. But in the light of other drift problems in the system it is evident that the contribution from the demodulator to the total error is negligible. The outputs from the amplifiers shows a small but constant DC offset which is easily compensated for in software. Measurement results can be found in section 5.1.6.

6.1.4 Frequency divider

The frequency divider that was designed and manufactured during the project works according to the expectations. Combined with the right filter the suppression of unwanted harmonics is better than $20\,dB$.

6.1.5 Characterisation of 30 GHz power amplifiers

The two power amplifiers used to pump the HBV multipliers in the HBV based measurement system, section 4.4, proved to deliver enough power for the application. The reason for investigation the amplifiers was that the used frequency range was outside of the amplifiers specified band. As seen through the measurement results in section 5.1.3 the gain needed in order to maintain a constant output power varies by several dB. Since the amplifiers operate close to the maximum input power the HBVs can handle it is practically challenging to feed two amplifiers at an optimal operating point when they are fed by the same source.

6.2 Optics

The results considering the optics design will be presented in this chapter.

6.2.1 Image reconstruction algorithm

The image reconstruction algorithm described in section 3.2.4 was chosen as the final method for image formation. Since the mechanical setup is not completed yet, no images have been created using the algorithm.

6.2.2 Quasi optical focusing

A simple gaussian telescope construction was proposed as an alternative for focusing in section 3.2.4. The design was not fully evaluated and has not been realised since the image reconstruction algorithm was chosen instead. Before realisation of the gaussian telescope approach it might be necessary to evaluate the beam distortion effects created by the focusing optics, it might be necessary to change some parameters in order to improve the shape of the focused spot.

6.2.3 Catadioptric lens

The measurements on the catadioptric lens showed that the lens needs to be redesigned for the specific frequency range in order to be used. The current version simply was to lossy.

6.3 Imaging

6.3.1 108 GHz scalar imaging

An envelope containing some items was imaged with the preceding system described in section 4.1. The result is presented in Figure 62 where two different raster scan resolutions are compared. The content of the envelope is shown in Figure 63.

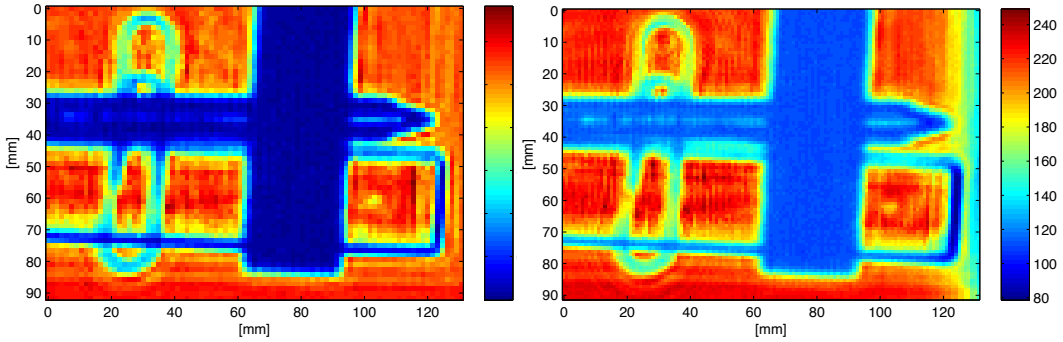

(a) Scan resolution $1,5mm$.

(b) Scan resolution $1mm$.

Figure 62: Two envelope scans with different scan resolution.

The scan reveals some interesting effects. At the border of the low loss ruler the measured signal power is low due to scattering at the sharp edge. The metallised razor blade package completely blocks the radiation, which was expected. The centre of the pencil shows a slightly lower attenuation, it is however uncertain if it is due to lower loss or diffraction from the hexagonal shape.

6.3.2 333 GHz imaging

Some examples of transmission imaging at $333\,GHz$ will be presented here. All images are produced using the system described in Section 4.2. A WR-03 waveguide probe is used on the receiver to define the spot size and the sample is illuminated using a WR-03 smooth-wall cylindrical horn. The colour bar in the pictures represent the received power in dBm.

Figure 64a shows a photo of four Alvedon tablets packaged in their original plastic wrapping. In Figure 64b the $333\,GHz$ transmission image is

Figure 63: Picture showing the contents of the envelope.

shown. Note that the tablets are homogenous but destructive interference makes the tablets appear more lossy around the edges. The small break-line can also be noted on all tablets in the small red centre section.

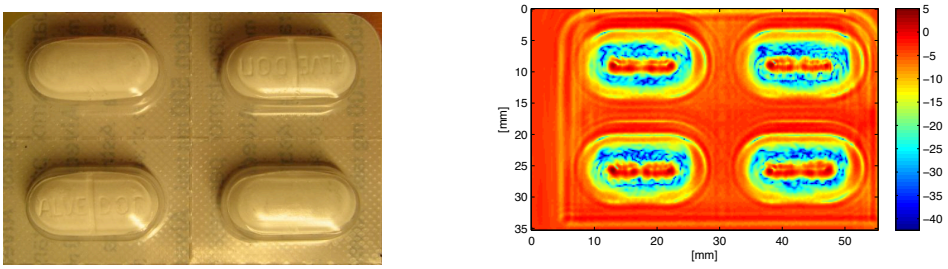

(a) Photograph of the tablets.

(b) 333 GHz transmission image.

Figure 64: Alvedon tablets.

Figure 65 shows a RFID door-key. In the centre of the device the RFID chip is clearly visible accompanied by its spiral antenna. Some plastic mold features add some extra information about the internal structure, visible as edge diffraction.

A 24 pin, 100 mil x 600 mil footprint, IC is reproduced both in visual spectrum and 333 GHz transmission in Figure 66. The chip in the centre is clearly visible accompanied by conducting traces and bond wires. The indentation in the epoxy package indicating pin 1 is also visible in the transmission image.

(a) Photograph of the RFID door-key.

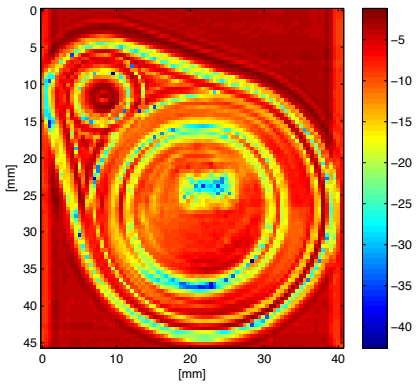

(b) 333 GHz transmission image.

Figure 65: Aptus RFID door-key.

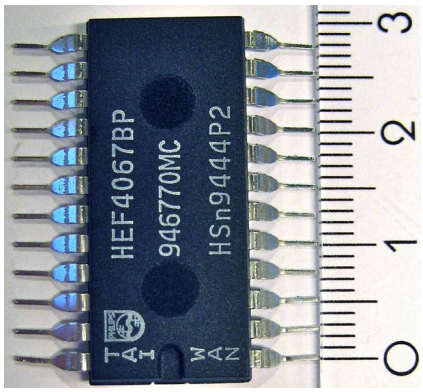

(a) Photograph of the IC circuit.

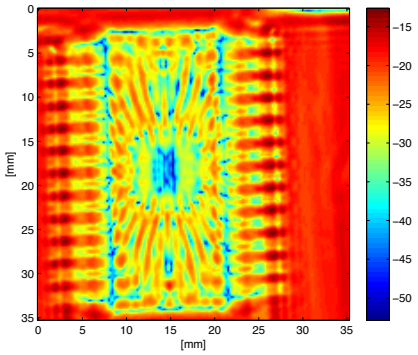

(b) 333 GHz transmission image.

Figure 66: Philips HEF4067BP IC circuit.

Figure 67a shows a cutout from Figure 66b and Figure 67b shows an image of the same area produced with the mechanical scan resolution set to 0.1 mm instead of 0.2 mm which is used in Figure 67a.

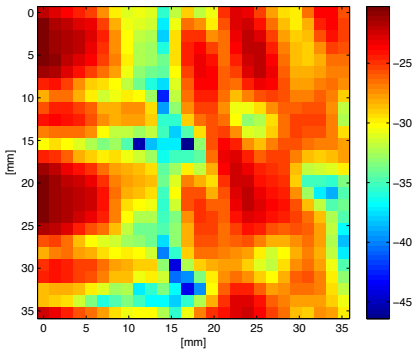

(a) 333GHz transmission image, mechanical resolution 0.2 mm, cutout from Figure 66b.

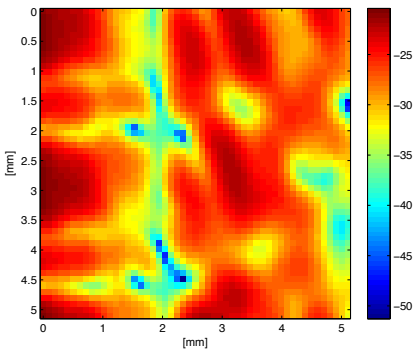

(b) 333GHz transmission image, mechanical resolution 0.1 mm.

Figure 67: A 5 mm x 5 mm comparison of different mechanical scan resolutions.

A freshly picked leaf revealed a surprisingly low water contents due to the fact that transmission imaging was possible. Figure 68b shows the transmission image where the thicker centre stem is visible along with other details.

(a) Photograph of leaf.

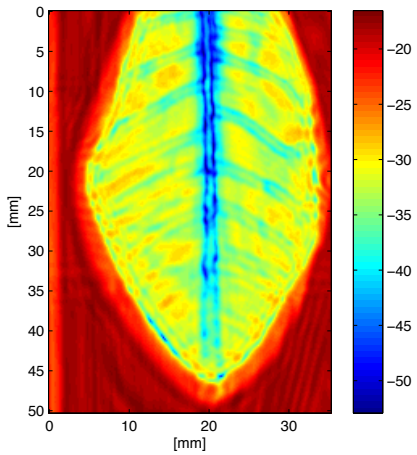

(b) 333 GHz transmission image.

Figure 68: Leaf.

Cancer samples obtained through the collaboration with Sahlgrenska have been imaged. However the samples adopted for transmission mi-

croscopy in the visible spectrum proved to be to thin to reveal any contrast. Instead a slowly varying pattern appeared which may be explained through either varying thickness of the mounting wax, a non constant sample glass thickness or standing waves. Figure 69a shows the mounting of the sample in the measurement system and Figure 69b shows the result from the scan.

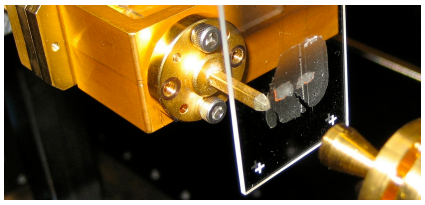

(a) Mounting of cancer sample in measurement setup.

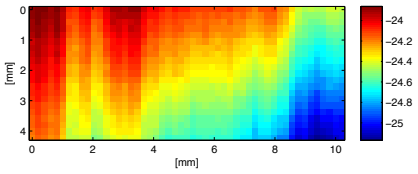

(b) 333 GHz transmission image.

Figure 69: One of the cancer samples obtained from Sahlgrenska.

In Figure 70 a slice o bacon has been imaged. It can be seen that the muscle tissue completely blocks the radiation while the fat is partly transmissive.

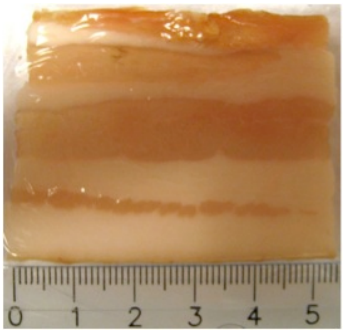

(a) Photograph of leaf.

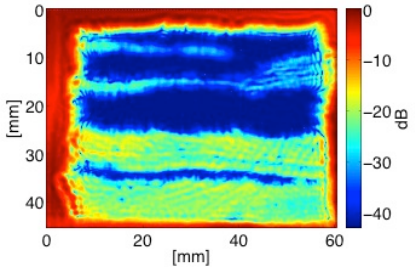

(b) 333 GHz transmission image.

Figure 70: Picture showing a slice of bacon.

6.3.3 Vector imaging

Using the Schottky based vector measurement system, section 4.3, an image of graphics printed in a laser printer was captured. The same mechanical setup as in the above measurements were used to perform the raster scan which took several hours. The image is resolvable both in the phase and amplitude, shown in Figure 71. The relatively small phase contrast, approximately 10°, confirms that the phase drift over several hours is small.

Figure 72 shows a photograph of the imaged print.

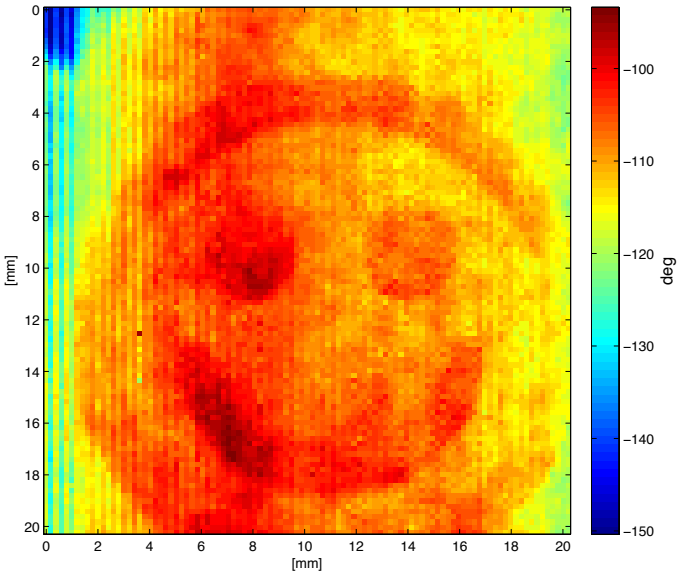

Figure 71: Phase contrast of the imaged laser print.

Figure 72: Photograph of the laser print.

6.4 Publications

During the period of the work two conference papers have been submitted, one for oral presentation at Lund GigaHertz Symposium 2010 and one for poster presentation at IRMMW-THz 2010 in Rome later this year. Both abstracts can be found in appended papers.

7 Conclusion and discussion

This section will present the conclusions drawn during the work both regarding what has been done and sub-millimetre wave imaging in general. Various aspects of the work as well as problems encountered will also be discussed.

An introduction to the part of the THz imaging area this project fall into was given in section 2.2.1. Most THz imaging systems in this category uses laser based terahertz pulsed imaging, one benefit of such systems is the large bandwidth in the order of hundreds of gigahertz. This eases the determination of the complex refractive index of the imaged object significantly. Dynamic range and spectral resolution is however two fields where multiplier based CW systems have an advantage.

The vector measurement system was successfully constructed along with components necessary in the IF chain. The bandwidth is currently limited by the LO bandwidth of the subharmonic Schottky mixer used. In the current design, which was not purposely designed for use in the imaging system, RF bandwidth was prioritised at the expense of LO bandwidth. Since the vector measurement setup uses a fixed frequency IF it does not benefit from such construction.

Concerning optics the two firstly considered alternatives, the catadioptric lens and the gaussian beam telescope, were abandoned in the middle of the work in favour for the image reconstruction technique. One of the reasons being a newly initiated collaboration with a department working in the field of microwave tomography algorithms.

In this work some examples of sub-millimetre wave images produced have been shown, future continuation of the work is however expected to deliver images using the image reconstruction algorithm described. The goal of showing the capabilities of the in house equipment is fulfilled.

The cell slides containing breast cancer tumours, obtained through Sahlgrenska, were adopted for optical transmission microscopy. Hence it has not been possible to create an image of the samples. When the measurement setup is finished new samples will be obtained and the experiment repeated.

The phase drift in the measurement system was found to be good in short term measurements and acceptable over longer periods, 90° during twelve hours.

Concerning the long term phase drift in the system a more thorough investigation needs to be done in order to investigate which components cause the largest drift. One candidate for high phase drift is the divider circuitry where the logical triggering level might drift with temperature and therefore trigger at different points of the sinusoidal input. However amplitude drift in the source feeding the divider would cause the same effect. A temperature stabilisation of firstly the IF chain but preferably also the sub-millimetre wave components is likely to reduce the problem.

Two conference papers have been published through the work but the aim is still to publish a journal article.

The field of THz imaging is far from fully developed and therefore many new applications are likely to be found. Current research is to a great extent aimed at security applications such as stand off detection of hidden weapons.

8 Future outlook

One goal of future work is to establish the microwave tomography algorithm in the sub-millimetre wave region. This will be done through a continued collaboration with the Biomedical Engineering Division, Department of Signals and Systems, Chalmers University of Technology.

Minimisation of electrical system drift is an other issue receiving attention, one alternative being thermal stabilisation of the measurement system.

The system bandwidth may be extended by improvements in the multiplier chains as well as by the use of a mixer with wider LO matching.

The work with finding new imaging applications in the sub-millimetre wave region will also continue.

References

[1] E Pickwell, B E Cole, A J Fitzgerald, M Pepper, and V P Wallace, "In vivostudy of human skin using pulsed terahertz radiation", *Phys. Med. Biol.*, vol. 49, no. 9, pp. 1595–1607, Apr 2004.

[2] R Appleby and HB Wallace, "Standoff detection of weapons and contraband in the 100 GHz to 1 THz region", *IEEE Transactions on Antennas and Propagation*, vol. 55, no. 11, pp. 2944, 2007.

[3] Wai Lam Chan, Jason Deibel, and Daniel M. Mittleman, "Imaging with terahertz radiation", *Reports on Progress in Physics*, vol. 70, no. 8, pp. 1325–1379, 2007.

[4] Peter H Siegel and Robert J Dengler, "Terahertz heterodyne imaging Part I: Introduction and techniques", *Int J Infrared Milli Waves*, vol. 27, no. 4, pp. 465–480, Jul 2007.

[5] Peter H Siegel and Robert J Dengler, "Terahertz Heterodyne Imaging Part II: Instruments", *Int J Infrared Milli Waves*, vol. 27, no. 5, pp. 631–655, Feb 2007.

[6] L Yujiri, M Shoucri, P Moffa, NGS Technol, and CA Redondo Beach, "Passive millimeter wave imaging", *IEEE microwave magazine*, vol. 4, no. 3, pp. 39–50, 2003.

[7] R.J Dengler, A Skalare, and P.H Siegel, "Passive and active imaging of humans for contraband detection at 640 GHz", *Microwave Symposium Digest, 2004 IEEE MTT-S International*, vol. 3, pp. 1591– 1594 Vol.3, 2004.

[8] E Gerecht, D Gu, L You, and KS Yngvesson, "A passive heterodyne hot electron bolometer imager operating at 850 GHz", *IEEE Transactions on Microwave Theory and Techniques*, vol. 56, no. 5 Part 1, pp. 1083–1091, 2008.

[9] Erik Öjefors, Alvydas Lisauskas, Diana Glaab, Hartmut G Roskos, and Ullrich R Pfeiffer, "Terahertz Imaging Detectors in CMOS Technology", *J Infrared Milli Terahz Waves*, pp. 1–12, Aug 2009.

[10] KB Cooper, RJ Dengler, G Chattopadhyay, E Schlecht, J Gill, A Skalare, I Mehdi, and PH Siegel, "A high-resolution imaging radar at 580 GHz", *IEEE Microwave and Wireless Components Letters*, vol. 18, no. 1, pp. 64–66, 2008.

[11] SynView GmbH, "www.synview.de".

[12] KB Cooper, RJ Dengler, N Llombart, T Bryllert, G Chattopadhyay, E Schlecht, J Gill, C Lee, A Skalare, and I Mehdi, "Penetrating 3-D Imaging at 4-and 25-m Range Using a Submillimeter-Wave Radar", *IEEE Transactions on Microwave Theory and Techniques*, vol. 56, no. 12, Part 1, pp. 2771–2778, 2008.

[13] Christian Am Weg, Wolff Von Spiegel, Ralf Henneberger, Ralf Zimmermann, Torsten Loeffler, and Hartmut G Roskos, "Fast Active THz Cameras with Ranging Capabilities", *J Infrared Milli Terahz Waves*, pp. 1–16, Aug 2009.

[14] Joo-Hiuk Son, "Terahertz electromagnetic interactions with biological matter and their applications", *J. Appl. Phys.*, vol. 105, no. 10, MAY 15 2009.

[15] BB HU and MC NUSS, "Imaging with terahertz waves", *Optics Letters*, vol. 20, no. 16, pp. 1716–&, Jan 1995.

[16] J. Axel Zeitler, Yaochun Shen, Colin Baker, Philip F Taday, Michael Pepper, and Thomas Rades, "Analysis of coating structures and interfaces in solid oral dosage forms by three dimensional terahertz pulsed imaging", *J Pharm Sci-Us*, vol. 96, no. 2, pp. 330–340, Jan 2007.

[17] ZD Taylor, RS Singh, MO Culjat, JY Suen, WS Grundfest, H Lee, and ER Brown, "Reflective terahertz imaging of porcine skin burns", *Optics Letters*, vol. 33, no. 11, pp. 1258–1260, 2008.

[18] KJ Siebert, T Loffler, H Quast, M Thomson, T Bauer, R Leonhardt, S Czasch, and HG Roskos, "All-optoelectronic continuous wave THz imaging for biomedical applications", *Phys. Med. Biol.*, vol. 47, no. 21, pp. 3743–3748, NOV 7 2002.

[19] V P Wallace and A J Fitzgerald, "Terahertz pulsed imaging o of human breast tumors", *Radiology*, vol. 239, no. 2, pp. 533–540, Apr 2006.

[20] AJ Fitzgerald, E Berry, NN Zinov'ev, S Homer-Vanniasinkam, RE Miles, JM Chamberlain, and MA Smith, "Catalogue of human tissue optical properties at terahertz frequencies", *Journal of Biological Physics*, vol. 29, no. 2, pp. 123–128, 2003.

[21] R.J Dengler, F Maiwald, and P.H Siegel, "A Compact 600 GHz Electronically Tunable Vector Measurement System for Submillimeter Wave Imaging", *Microwave Symposium Digest*, pp. 1923–1926, 2006.

[22] JL Doane, "Broadband superheterodyne tracking circuits for millimeterwave measurements", *Review of Scientific Instruments*, vol. 51, pp. 317, 1980.

[23] Biddut Banik, Josip Vukusic, and Jan Stake, "Millimeter wave characterization of a catadioptric lens for imaging applications", *IEEE Microwave and Wireless Components Letters*, vol. 19, no. 11, pp. 680–682, Jan 2009.

[24] F Biraud and G Daigne, "Achromatic doublets for gaussian beams", *Antennas and Propagation, IEEE Transactions on*, vol. 39, no. 4, pp. 559 – 562, Apr 1991.

[25] P. F. Goldsmith, *Quasioptical Systems*, IEEE Press, Chapman & Hall, 1998.

[26] Matteo Pastorino, *Microwave Imaging*, John Wiley & Sons, Inc., 2010.

[27] P Sobis, T Bryllert, AØ Olsen, and J Vukusic, "Compact 340 GHz Receiver Front-Ends", *ISSTT*, 2009.

[28] T.W Crowe, W.L Bishop, D.W Porterfield, J.L Hesler, and R.M Weikle, "Opening the terahertz window with integrated diode circuits", *IEEE Journal of Solid-State Circuits*, vol. 40, no. 10, pp. 2104– 2110, 2005.

A Appended papers

- R. Dahlbäck, B. Banik, P. Sobis, A. Fhager, M. Persson, and J. Stake, "A Compact 340 GHz Heterodyne Imaging System,"presented at the GigaHertz 2010, Lund, March 2010.

- R. Dahlbäck, T. Rubaek, T. Bryllert, M. Persson, and J. Stake, "A 340 GHz CW non-linear imaging system,"to be presented at IRMMW-THz, Rom, September 2010.

A Compact 340 GHz Heterodyne Imaging System

Robin Dahlbäck[1], Biddut Banik[1], Peter Sobis[3], Andreas Fhager[2], Mikael Persson[2] and Jan Stake[1]

[1]Physical electronic Laboratory, Department of Microtechnology and Nanoscience,
[2]Biomedical Engineering Division, Department of Signals and Systems,
Chalmers University of Technology, SE-412 96 Göteborg, Sweden.
[3]Omnisys Instruments AB
Email: dahlback@chalmers.se

I. Introduction and Background

Terahertz (THz, 10^{12} Hertz) imaging has attracted a lot of attention recently in various applications ranging from production process control to breast cancer imaging [1]. However, those practical applications require compact sources and systems offering room temperature operation. Contrary to time domain systems, continuous wave (CW) imaging systems are usually compact, simple, fast, and of relatively low-cost. High spectral resolution is another advantage. A common approach for realizing CW THz systems is up-conversion from microwave frequencies using frequency multipliers for signal generation and sub-harmonic mixers for detection [2].

We present a RT CW imaging setup operating around 340 GHz that consists of a multiplier chain and a receiver chain, shown in Fig. 1. The system provides heterodyne detection with an IF BW of 0-20 GHz with the possibility of extracting the phase information. Furthermore, the system utilizes the ultra-compact catadioptric lens for short range imaging applications.

The previous setup, described in [3], operated in direct detection mode at around 100 GHz. A catadioptric lens-horn combination was used as a focusing element producing a marked improvement in image resolution. However, the setup was based on direct detection technique and the phase information was missing. Therefore the setup was not able to resolve dielectric contrast. Moreover, the slow response time of the detector also limited the imaging speed.

The 340 GHz imaging setup, described here, is a heterodyne system and aims at collecting vector measurement data in order to improve image detail. For instance in biomedical applications this provides an advantage over scalar measurements. The system uses a sub-harmonic RT Schottky mixer as receiver [4]. Two separate multiplier chains are used to generate the LO drive and illumination signal.

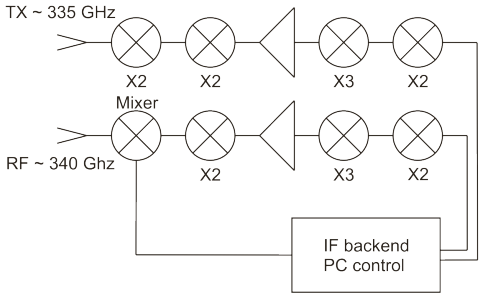

Fig. 1 Block diagram of the 340 GHz heterodyne imaging system.

II. Results

The system, shown in Fig. 2, is completely automated with 3-axis positioning stage and data acquisition. Being heterodyne in nature, the setup provides fast data acquisition and imaging speed. We will present detailed characterization results regarding beam diameter, spatial resolution and dynamic range. Furthermore, the setup will be employed for various applications including biomedical and object investigation and results will be presented.

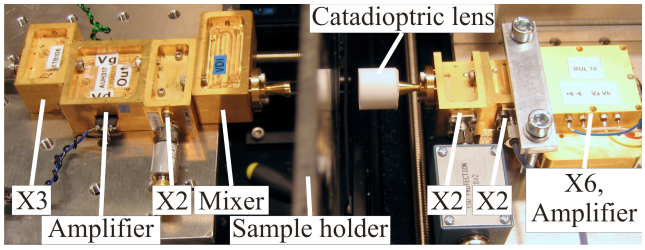

Fig. 2 The constructed 340 GHz heterodyne imaging setup in transmission-mode.

References

[1] Chan W.L., Deibel J., Mittleman D.M., "Imaging with terahertz radiation", *Rep. Prog. Phys*, vol.70, pp.1325-1379, 2007.

[2] Dengler, R.J.; Maiwald, F.; Siegel, P.H., "A Compact 600 GHz Electronically Tunable Vector Measurement System for Submillimeter Wave Imaging," *Microwave Symposium Digest, 2006. IEEE MTT-S International* , pp.1923-1926, 11-16 June 2006

[3] Banik, B.; Vukusic, J.; Stake, J., "Millimeter Wave Characterization of a Catadioptric Lens for Imaging Applications," *IEEE Microwave and Wireless Components Letters,* vol.19, no.11, pp.680-682, Nov. 2009.

[4] Sobis P., Bryllert T., Olsen A.Ø., Vukusic J., Drakinskiy V., Cherednichenko S., Emrich A., Stake J., "Compact 340 GHz Receiver Front-Ends", *ISSTT*, 2009

A 340 GHz CW non-linear imaging system

Robin Dahlbäck[a], Tonny Rubaek[b], Tomas Bryllert[a], Mikael Persson[b] and Jan Stake[a]
[a]Physical Electronic Laboratory, Department of Microtechnology and Nanoscience,
[b]Biomedical Engineering Division, Department of Signals and Systems,
Chalmers University of Technology, SE-412 96 Göteborg, Sweden.

***Abstract*—A CW sub-millimeter wave imaging system is presented. The system operates around 340GHz and uses a non-linear imaging algorithm.**

I. Introduction And Background

IMAGING applications in the sub-millimeter wave region is a topic that has attracted a lot of attention in recent years. Common topologies include laser-based systems utilizing photoconductive effects as well as solid-state multiplier systems. The imaging algorithms are commonly based on linear approaches such as in the quasi-optical approaches for scanning larger areas e.g. in security applications and near-field imaging used for microscopy [1].

In this paper, the THz imaging system currently being developed at Chalmers University of Technology is presented. The system operates in continuous-wave (CW) mode and a nonlinear algorithm is used for reconstructing the images.

A common approach for realizing CW THz systems is up-conversion from microwave frequencies using frequency multipliers for signal generation and sub-harmonic mixers for detection [2].

We present a room temperature (RT) CW imaging setup operating around 340 GHz that consists of a multiplier chain and a receiver chain, shown in Fig. 1. The system provides heterodyne detection with the possibility of extracting the phase information, thus enabling non-linear imaging algorithms.

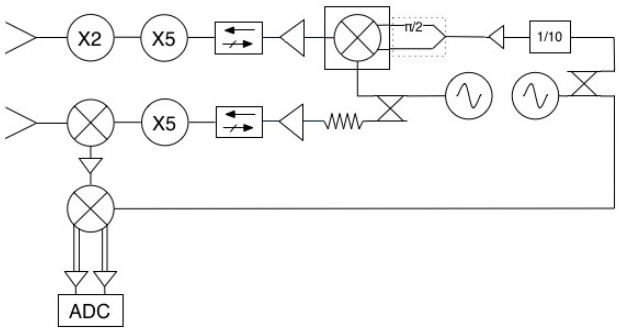

Fig. 1 Block diagram of the 340GHz imaging system.

The system uses a sub-harmonic RT Schottky mixer as receiver [3]. Two separate multiplier chains, consisting of hetero structure barrier varactor (HBV) and Schottky multipliers are used to generate the LO drive and illumination signal.

The imaging algorithm used in the system is based on full non-linear inversion. This technique has been used for some time for imaging in the microwave region, but has not yet found widespread application in the THz domain [4]. In this system, a Newton-type algorithm is applied for solving the nonlinear minimization problem

$$\underline{\varepsilon} = \operatorname{argmin}\left\{\left\|\underline{S}^{meas} - \underline{S}^{calc}\left(\underline{\varepsilon}\right)\right\|_2\right\}$$

Here, $\underline{\varepsilon}$ is a discrete representation of the unknown complex permittivity of the imaging domain, and $\underline{S}^{meas}$ and $\underline{S}^{calc}$ are vectors holding the measured and calculated S parameters, respectively.

II. Results

Results from measurements using the above system will be presented together with information about the modeling. Furthermore, system characterization data will be presented.

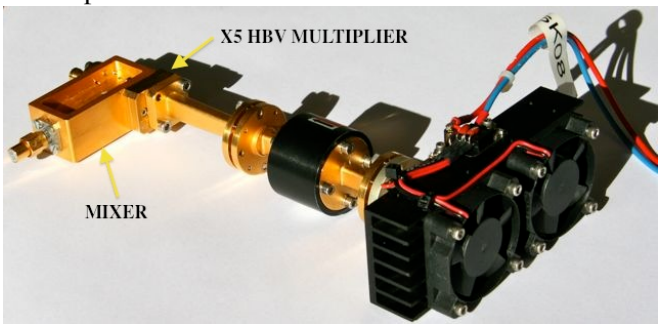

Fig. 2 Photograph of the receive chain.

References

[1] W. L. Chan, J. Deibel, D. M. Mittleman, "Imaging with terahertz radiation", *Rep. Prog. Phys.*, 2007, Vol 70, pp. 1325-1379.

[2] R. J. Dengler, F. Maiwald, P. H. Siegel, "A Compact 600 GHz Electronically Tunable Vector Measurement System for Submillimeter Wave Imaging", *Microwave Symposium Digest, 2006. IEEE MTT-S International*, pp. 1923-1926, 11-16 June 2006

[3] P. Sobis, T. Bryllert, A. Ø. Olsen, J. Vukusic, V. Drakinskiy, S Cherednichenko, A. Emrich, J. Stake, "Compact 340 GHz Receiver Front-Ends", *ISSTT*, 2009

[4] T. Rubaek, O. S Kim, P. Meincke, "Computational Validation of a 3-D Microwave Imaging System for Breast-Cancer Screening", *IEEE Trans. on Antennas and Propagation,* 2009, Vol 57, pp. 2105-2115.

B PCB layouts

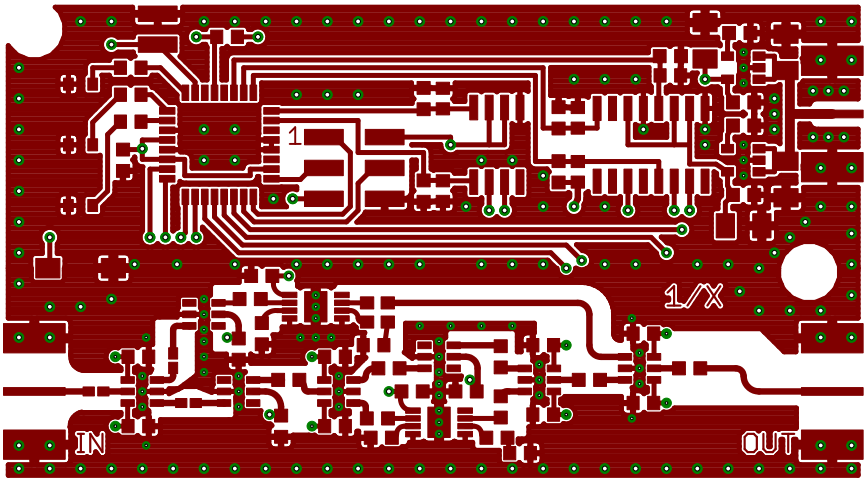

Figure 73: Top layer.

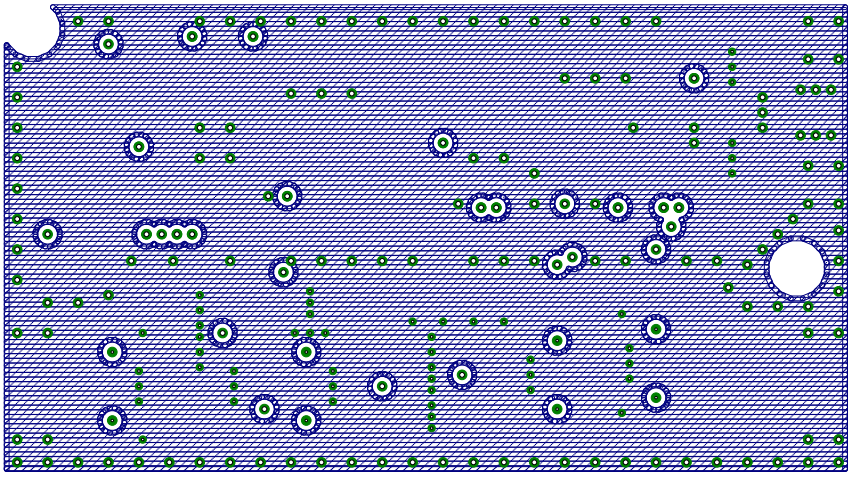

Figure 74: Inner layer 1.

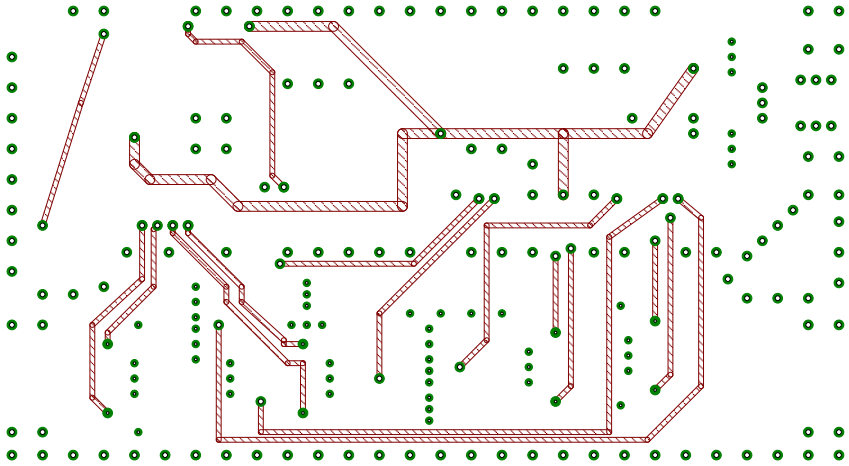

Figure 75: Inner layer 2.

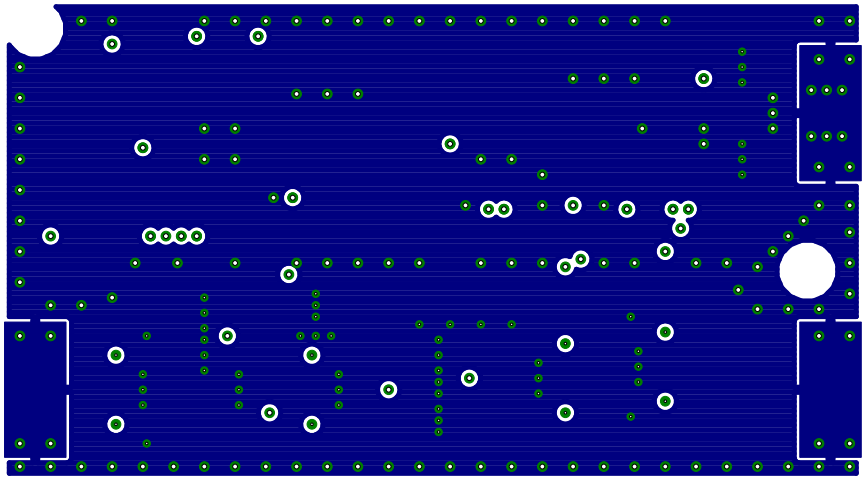

Figure 76: Bottom layer.